latitude variation is rarely > 6 nT/km. Thus elevation and latitude corrections are generally unnecessary.

The influence of topography on ground magnetics, on the other hand, can be very important. This is apparent when taking measurements in stream gorges, for example, where the rock walls above the station frequently produce abnormal magnetic lows. Terrain anomalies as large as 700 nT occur at steep (45°) slopes of only 10 m extent in formations containing 2% magnetite ($k = 0.025$ SI unit) (Gupta and Fitzpatrick, 1971). In such cases, a terrain correction is required, but it cannot be applied merely as a function of topography alone because there are situations (for example, sedimentary formations of very low susceptibility) in which no terrain distortion is observed.

A terrain smoothing correction may be carried out by reducing measurements from an irregular surface $z = h(x, y)$ to a horizontal plane, say $z = 0$, above it. This can be done approximately by using a Taylor series (§A.5) with two terms:

$$Z(x, y, 0) = Z(x, y, h) - h(\partial Z/\partial z)_{z=h} \quad (3.33)$$

3.5.5. Gradiometer Surveys

The gradient of F is usually calculated from the magnetic contour map with the aid of templates. There is, however, considerable merit in measuring the vertical gradient directly in the field. It is merely necessary to record two readings, one above the other. With instrument sensitivity of 1 nT, an elevation difference of ≈ 1 m suffices. Then the vertical gradient is given by

$$\partial F/\partial z = (F_2 - F_1)/\Delta z$$

where F_1 and F_2 are readings at the higher and lower elevations, and Δz is the separation distance.

Discrimination between neighboring anomalies is enhanced in the gradient measurements. For example, the anomalies for two isolated poles at depth h separated by a horizontal distance h yield separate peaks on a $\partial F/\partial z$ profile but they have to be separated by 1.4 h to yield separate anomalies on an F profile. The effect of diurnal variations is also minimized, which is especially beneficial in high magnetic latitudes. For most of the simple shapes discussed in Section 3.6 (especially for the isolated pole, finite-length dipole, and vertical contact of great depth extent), better depth estimates can be made from the first vertical-derivative profiles than from either the Z or F profiles. For features of the first two types, the width of the profile at $(\partial Z/\partial z)_{max}/2$ equals the depth within a few percent. For the vertical contact, half the separation between maximum and minimum values equals the depth. Gradiometer measurements are valuable in field continuation calculations (§3.7.5).

Ground gradiometer measurements (Hood and McClure, 1965) have recently been carried out for gold deposits in eastern Canada in an area where the overburden is only a few meters thick. The host quartz was located because of its slightly negative susceptibility using a vertical separation of 2 m and a station spacing of ≈ 1 m. Gradiometer surveys have also been used in the search for archeological sites and artifacts, mapping buried stone structures, forges, kilns, and so forth (Clark, 1986; Wynn, 1986).

Vertical gradient aeromagnetic surveys (Hood, 1965) are often carried out at 150 to 300 m altitude. Detailed coverage with 100 to 200 m line spacing is occasionally obtained at 30 m ground clearance.

Two magnetometers horizontally displaced from each other are also used, especially with marine measurements where they may be separated by 100 to 200 m. This arrangement permits the elimination of rapid temporal variations so that small spatial anomalies can be interpreted with higher confidence.

3.6. MAGNETIC EFFECTS OF SIMPLE SHAPES

3.6.1. General

Because ground surveys (until about 1968) measured the vertical-field component, whereas airborne surveys measured the total field, both vertical-component and total-field responses will be developed. Depth determinations are most important and lateral extent less so, whereas dip estimates are the least important and quite difficult. In this regard, aeromagnetic and electromagnetic interpretation are similar. In petroleum exploration the depth to basement is the prime concern, whereas in mineral exploration more detail is desirable. The potentialities of high resolution and vertical-gradient aeromagnetics are only now being exploited to a limited extent.

As in gravity and electromagnetics, anomalies are often matched with models. The magnetic problem is more difficult because of the dipole character of the magnetic field and the possibility of remanence. Very simple geometrical models are usually employed: isolated pole, dipole, lines of poles and dipoles, thin plate, dike (prism), and vertical contact. Because the shape of magnetic anomalies relates to the magnetic field, directions in the following sections are with respect to magnetic north (the x direction), magnetic east, and so forth, the z axis is positive downward, and we assume that locations are in the northern hemisphere. We use I for the field inclination, ξ for

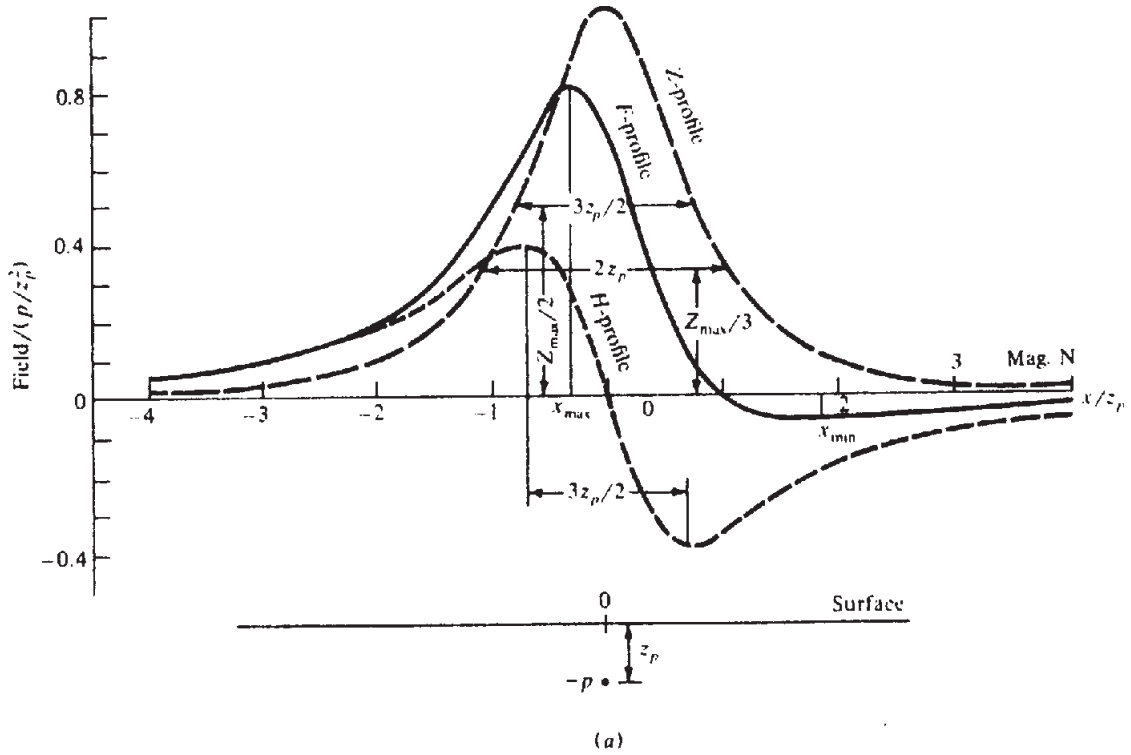

Figure 3.14. Magnetic effects of an isolated pole. (a) F, Z, and H profiles for $I = 45°$.

the dip of bodies and β for the strike angle relative to magnetic north (x axis). Note that depths are measured with respect to the measurement elevation (the aircraft elevation for aeromagnetic measurements).

3.6.2. The Isolated Pole (Monopole)

Although an isolated pole is a fiction, in practice it may be used to represent a steeply dipping dipole whose lower pole is so far away that it has a negligible effect. The induced magnetization in a long, slender, near-vertical body tends to be along the axis of the body except near the magnetic equator. If the length of the body is large, we have, in effect, a single negative pole $-p$ located at $(0, 0, z_p)$.

From Equation (3.2) or Equations (3.9) and (3.11), we get for the field at $P(x, y, 0)$,

$$\mathbf{F}_p = \left(-p/r^2\right)\mathbf{r}_1 = \left(p/r^3\right)\left(-x\mathbf{i} - y\mathbf{j} + z_p\mathbf{k}\right)$$

where $\mathbf{r}_1$ is a unit vector from $P(x, y, 0)$ toward the pole $-p$. The vertical anomaly is

$$Z = \left(pz_p/r^3\right) \qquad (3.34a)$$

Usually the field of the pole, $\mathbf{F}_p$, is much smaller than the field of the Earth, $\mathbf{F}_e$, and the total field anomaly is approximately the component of $\mathbf{F}_p$ in the $\mathbf{F}_e$ direction. Using Equation (3.29),

$$F \approx \mathbf{F}_p \cdot \mathbf{f}_1 = \left(p/r^3\right)\left(-x\cos I + z_p \sin I\right) \qquad (3.34b)$$

[Note that the total field anomaly F, which is only a component of $\mathbf{F}_p$, may be smaller than Z, and that in general $F \neq (Z^2 + H^2)^{1/2}$.]

Profiles are shown in Figure 3.14a for $I = 45°$; Z_{max} is located directly over the pole. The H profile is perfectly asymmetric and its positive half intersects the Z profile nearly at $Z_{max}/3$. The horizontal distance between positive and negative peaks of H is approximately $3z_p/2$. This profile is independent of the traverse direction only if the effect of the pole is much larger than the horizontal component of the Earth's field.

A set of total-field profiles for various values of I is shown in Figure 3.14c. F_{max} occurs south of the monopole and F_{min} north of it. F is zero north of the pole at $x = z \tan I$. The curves would be reflected in the vertical axis in southern latitudes. A total-field profile on a magnetic meridian becomes progressively more asymmetric as the inclination decreases (that is, as we move toward the magnetic equator). At the same time, the maximum decreases and the minimum increases and both are displaced progressively southward. The statement also applies

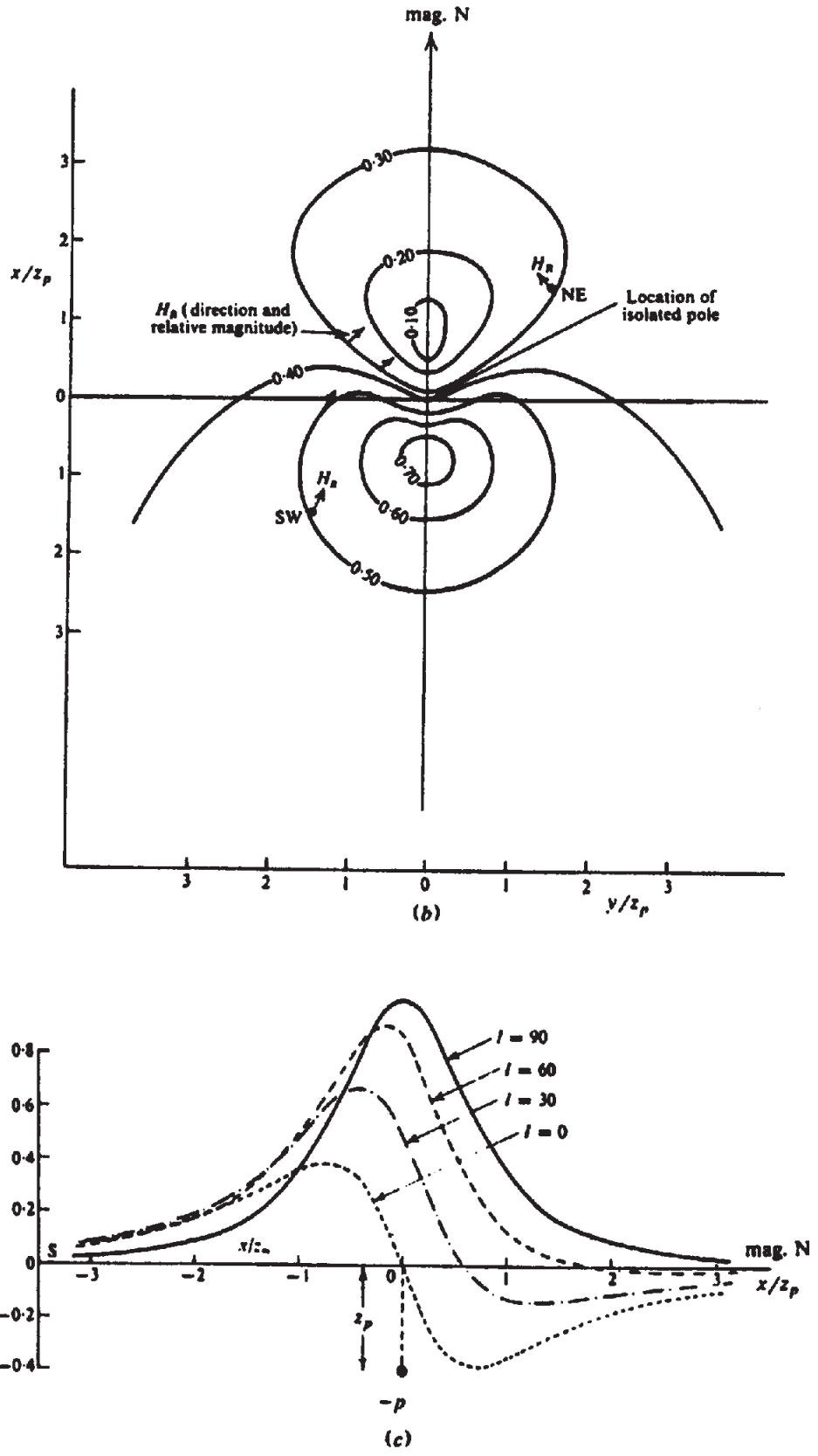

Figure 3.14. (Continued) (b) Contours of $|\mathbf{H}_R| = |\mathbf{H} + \mathbf{H}_e|$ *for* $\mathbf{H}_{max} = \mathbf{H}_e = 0.38$. *(c) F profiles for various inclinations. (After Smellie, 1967.)*

to the southern hemisphere if we interchange maximum and minimum.

The maximum and minimum values of F in Equation (3.34b) occur at

$$x_{max,\,min} = z_p\left\{3 \pm (9 + 8\cot^2 I)^{1/2}\right\}/4\cot I \qquad (3.35a)$$

where the plus sign gives F_{max}. The maximum and minimum values of F (recalling that the pole is $-p$, hence p is positive) are

$$F_{max,\,min} = \left(p \sin I/4z_p^2\right)\left\{1 \pm (9 + 8\cot^2 I)^{1/2}\right\}/\left\{1 + \left(x_{max,\,min}/z_p\right)^2\right\}^{3/2} \qquad (3.35b)$$

There are several relations between the profile characteristics and the pole depth. When $Z = Z_{max}/2$, $x_{1/2} = 0.75z_p$ (Fig. 3.14a), and when $Z = Z_{max}/3$, $x_{1/3} = z_p$, where $x_{1/2}$ and $x_{1/3}$ are the half-widths at $Z_{max}/2$ and $Z_{max}/3$, respectively. Pole depth may also be estimated from Equations (3.35). For example,

$$z_p = 2(x_{min} - x_{max})/(8 + 9\tan^2 I)^{1/2} \qquad (3.36a)$$

$$= 4(x_0 - x_{max})/\left\{\tan I + (8 + 9\tan^2 I)^{1/2}\right\} \qquad (3.36b)$$

It may be difficult to locate x_{min} and x_0 in high latitudes, however, since the curves are practically symmetrical when $I > 60°$. An alternative estimate, good within 10%, is given by $z_p \approx 1.4x_{1/2}$, where $x_{1/2}$ is the half-width of the F profile.

A first vertical-derivative profile provides a good depth estimate. The width of the profile at $(1/2)(\partial Z/dz)_{max}$ is equal to z_p to within a few percent.

3.6.3. The Dipole

A small three-dimensional structure containing anomalous concentrations of magnetic materials and varying in section from rod-like to spherical often may be represented by a dipole model. The dipole field was developed in Section 3.2.3. Assuming that a structure is magnetized mainly by induction in the direction of the Earth's field, the dipole dip will be that of the inclination, and the magnetic response may be obtained from Equation (3.14). If the body's intrinsic field due to remanence is much larger than the external field (an unlikely case), the magnetic response may also be obtained from these equations, replacing the inclination I with the dip of the dipole ξ.

Figure 3.15a shows the geometry. For a traverse in the dip direction, we find F, H, and Z by resolving F_r and F_θ in Equation (3.14a) along the dipole, the vertical, and the horizontal directions, respectively. Thus,

$$\begin{aligned} F &= F_r\cos\theta - F_\theta\sin\theta = (m/r^3)(3\cos^2\theta - 1) \\ &= (m/r^3)\left\{3\cos^2(I + \phi) - 1\right\} \\ &= (m/r^5)\left\{(3\cos^2 I - 1)x^2 - 6xz_m \sin I\cos I \right. \\ &\qquad \left. + (3\sin^2 I - 1)z_m^2\right\} \end{aligned} \qquad (3.37a)$$

$$\begin{aligned} Z &= -(F_r\sin\phi + F_\theta\cos\phi) \\ &= -(m/r^3)(2\cos\theta\sin\phi + \sin\theta\cos\phi) \\ &= (m/r^5)\left\{(2z_m^2 - x^2)\sin I - 3xz_m\cos I\right\} \end{aligned} \qquad (3.37b)$$

$$\begin{aligned} H &= F_r\cos\phi - F_\theta\sin\phi \\ &= (m/r^3)(2\cos\theta\cos\phi - \sin\theta\sin\phi) \\ &= (m/r^5)\left\{(2x^2 - z_m^2)\cos I - 3xz_m\sin I\right\} \end{aligned} \qquad (3.37c)$$

where $m = 2pl$ and z_m is the depth of the dipole below the surface of measurement.

Profiles are shown in Figure 3.15b for $I = 45°$. The dipole curves are somewhat sharper than for the monopole. The width, x^*, of the Z curves in Figure 3.15b at $\sim Z_{max}/2$ is $x^* \approx z_m$. The same relation holds for the F curves in Figure 3.15b, e in the range $30° \le I \le 90°$. For $I = 0$, however, the profile is sharper and $x^* \approx 0.7z_m$ at $F_{max}/2$. The F and Z profiles would be symmetrical on E–W traverses, with the flanks asymptotic to zero. The width of a gradiometer profile peak at $(1/2)(\partial Z/\partial z)_{max}$ gives a good estimate of z_m.

When the dipole is polarized approximately vertically, which would be the case where $I \ge 70°$, we have

$$F \approx Z = m(2z_m^2 - x^2)/r^5 \quad \text{and} \quad H = -3mxz_m/r^5 \qquad (3.38a)$$

Near the magnetic equator, $I \approx 0$ and

$$F \approx H = m(2x^2 - z_m^2)/r^5 \quad \text{and} \quad Z = -3mxz_m/r^5 \qquad (3.38b)$$

Curves for these limiting cases are shown in Figure 3.15c and d.

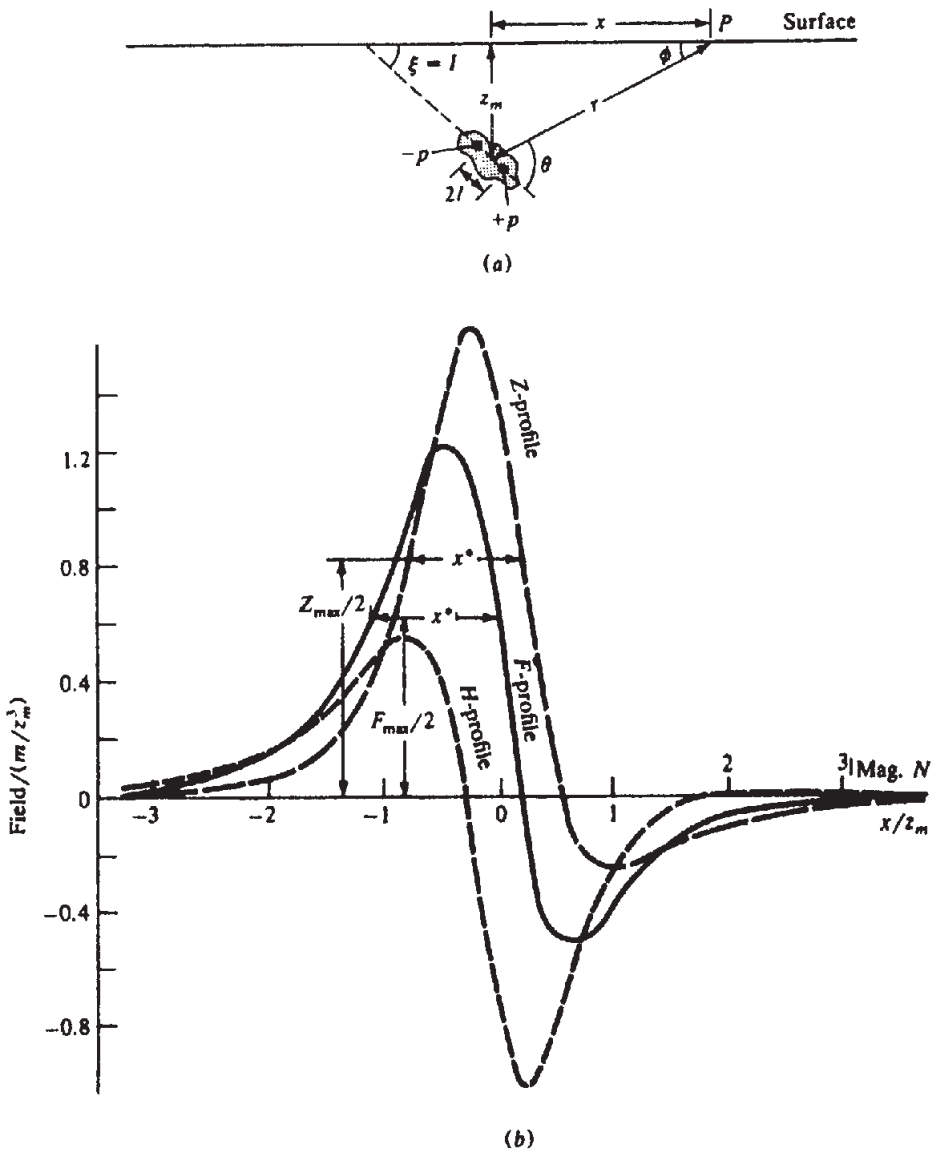

Figure 3.15. Magnetic effects of an isolated dipole. (a) Geometry. (b) Profiles for $I = 45°$.

The following relations hold for the vertical dipole:

$$\left.\begin{aligned} &\text{At } x = 0,\ Z, F \text{ are maxima:} \\ &\qquad Z_{max} = F_{max} = 2m/z_m^3 \\ &\text{At } x = \pm 2z_m,\ Z, F \text{ are minima:} \\ &\qquad Z_{min} = F_{min} = -0.036m/z_m^3 \\ &\text{At } x = \pm z_m\sqrt{2} \qquad Z = F = 0 \end{aligned}\right\} \quad (3.39a)$$

Similar relations hold for the horizontal dipole:

$$\left.\begin{aligned} &\text{At } x = 0, && H_{min} = F_{min} = -m/z_m^3 \\ &\text{At } x = \pm 1.2z_m, && H_{max} = F_{max} = 0.20m/z_m^3 \\ &\text{At } x = \pm z_m/\sqrt{2}, && H = F = 0 \end{aligned}\right\} \quad (3.39b)$$

The direction of dipole dip is toward the side of the Z profile that has the steeper slope and negative tail. This tail is not pronounced, however, unless the dip $\xi < 50°$. The F profiles are even more diagnostic of dip. In Figure 3.15d the Z profile is asymmetrical, with peak and trough above the ends of a long dipole for $z_m/l \ll 2$. When $z_m/l > 1$, the peak and trough occur beyond the ends and depth cannot be estimated, although a steep slope at the zero crossover would indicate a shallow source.

A finite dipole sometimes may be represented by a dipping sheet of finite length and depth extent [Eq. (3.58)] or by an infinite vertical dipping dike of finite strike length [Eq. (3.49)].

3.6.4. Two-Dimensional Features

(a) General. Clearly the strike of a two-dimensional feature with respect to the earth's field will

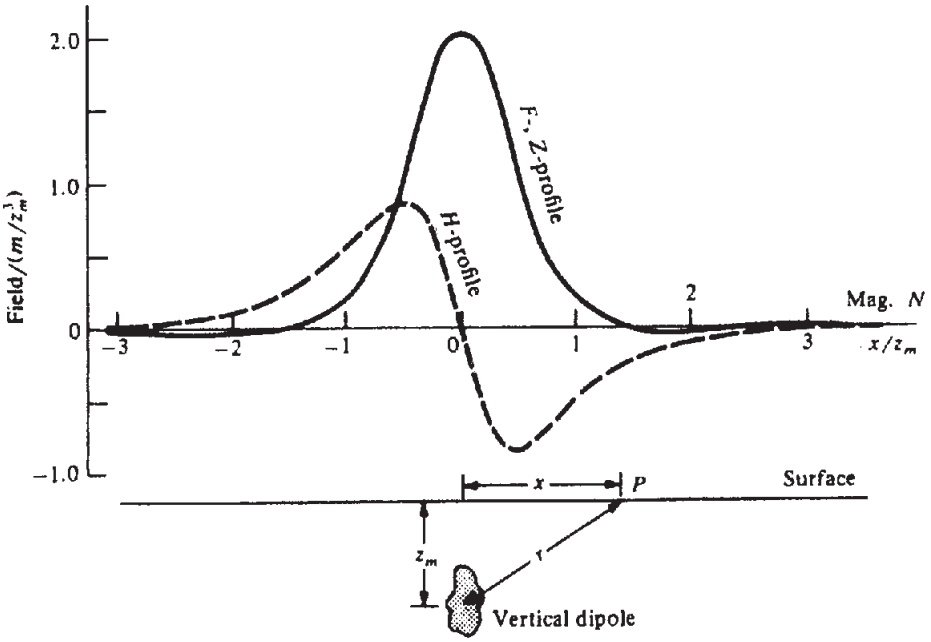

(c)

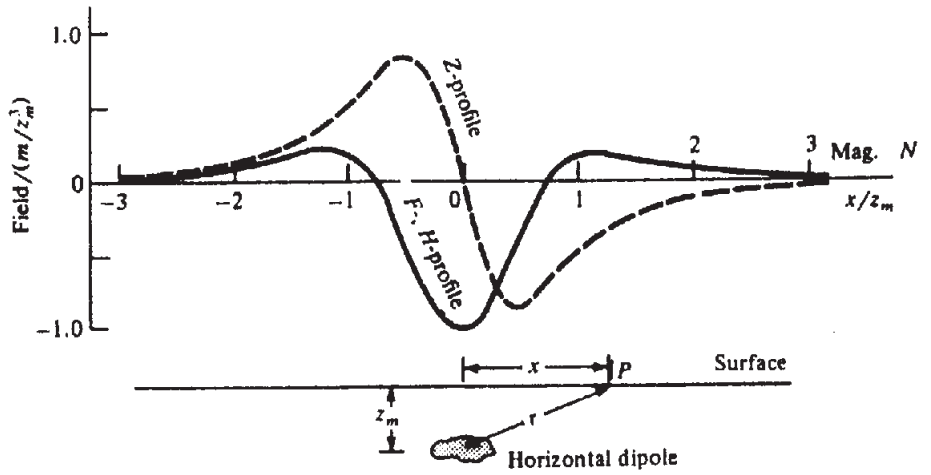

(d)

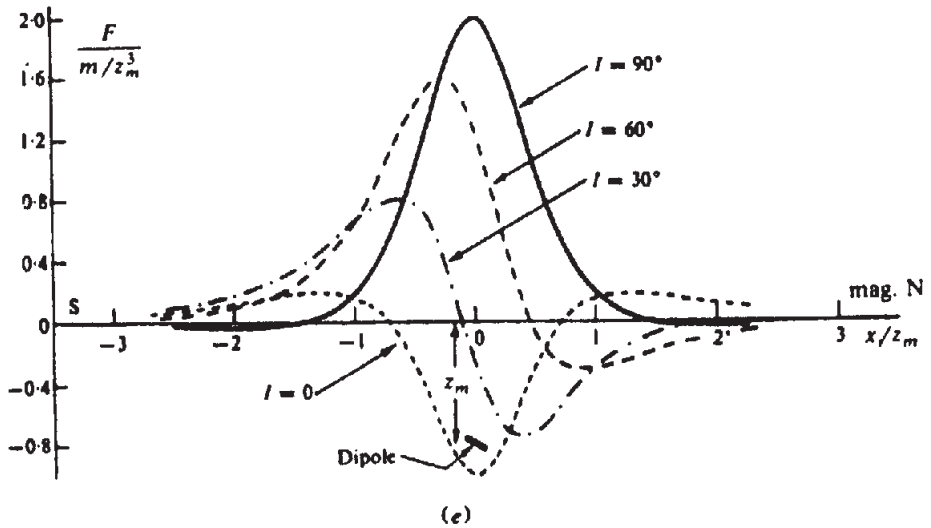

(e)

Figure 3.15. (Continued) (c) Profiles for vertical dipole. (d) Profiles for horizontal dipole. (e) F profiles for different inclinations of field and dipole. (After Smellie, 1967.)

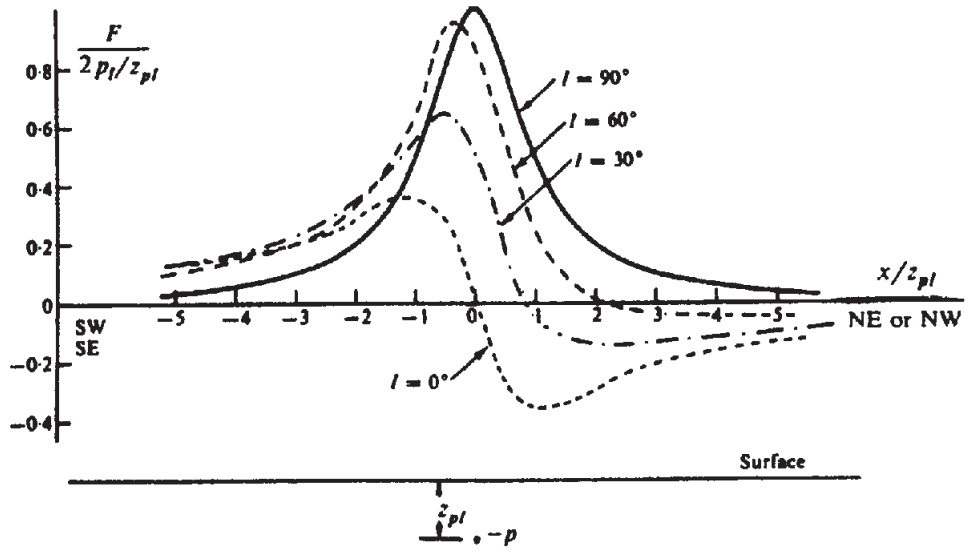

Figure 3.16. Total-field profiles normal to a line of poles striking NW–SE.

control induced magnetization, so the strike direction β will be incorporated in the expressions for various structures. Traverse direction is more critical in identifying a 2-D target. A profile approximately along strike will be unproductive. For 2-D models, it is customary to exhibit only *principal profiles* (normal to strike of the bodies). As in gravity, a magnetic body generally is considered to be 2-D when its strike length is at least 10 to 20 times larger than other dimensions. This situation is even less likely to be true in magnetics than it is in gravity, and formulas are often modified for finite strike length (Rasmussen and Pedersen, 1979).

In addition to using direct magnetic analysis, 2-D features may also be derived with relative ease from the corresponding gravity shapes by using Poisson's relation (§3.2.5).

(b) Line of poles (thin vertical dike of infinite depth extent). An infinite horizontal line of poles is an approximation to a long shear or fracture zone or thin dike, which has appreciable susceptibility contrast and which extends to considerable depth. The magnetic potential is given by the logarithmic relation $A = -2p_l \ln(1/r)$, where $-p_l$ is the pole intensity per unit length [this equation comes from Eq. (3.9) following the procedure in problem 1, Chapter 2, and assuming infinitesimal cross section in Eq. (2.8)]. We pass a vertical plane through $P(x, y, 0)$ perpendicular to the line of poles and take x' and z' axes in this plane such that x' is horizontal, $z' = z$, and the line of poles intersects the z axis at a depth z_{pl}. β is the angle between the x and $-y'$ axes. The field $\mathbf{F}_{pl}$ is in this plane and is directed down from P toward the line of poles along the vector $\mathbf{r} = (-x'\mathbf{i}' + z_{pl}\mathbf{k})$. To get derivatives of r at P, we write r^2 in terms of the components of r and temporarily replace $P(x',0)$ with $P'(x', z)$. Then, $r^2 = (-x')^2 + (z_{pl} - z)^2$, $\partial r/\partial x = x'/r$, and $\partial r/\partial z = \lim_{z\to 0}\{-(z_{pl} - z)/r\} = -z_{pl}/r$. Then,

$$\begin{aligned}\mathbf{F}_{pl} &= -\nabla A = -2p_l \nabla\{\ln r\} \\ &= (2p_l/r^2)(-x'\mathbf{i}' + z_{pl}\mathbf{k}) \\ &= (2p_l/r^2)(-x' \sin\beta\mathbf{i} + z_{pl}\mathbf{k}) \quad (3.40a)\end{aligned}$$

Now the component along $\mathbf{F}_e$ is

$$\begin{aligned}F &= \mathbf{F}_{pl} \cdot \mathbf{f}_1 \\ &= (2p_l/r^2)(-x' \sin\beta\mathbf{i} + z_{pl}\mathbf{k}) \\ &\quad \cdot(\cos I\mathbf{i} + \sin I\mathbf{k}) \\ &= (2p_l/r^2)(-x' \cos I \sin\beta + z_{pl} \sin I) \quad (3.40b)\end{aligned}$$

where $r^2 = x'^2 + z_{pl}^2$. The vertical component is

$$Z = 2p_l z_{pl}/r^2 \quad (3.40c)$$

The north–south component of H is from Equation (3.40a):

$$H = -(2p_l/r^2)x' \sin\beta \quad (3.40d)$$

Total-field principal profiles (normal to strike) are shown in Figure 3.16 for several inclinations and strike $\beta = 45°$. Obviously the Z profiles are the same for any strike direction. The F curves in Figure 3.16 have the same character as for the single pole, although they are somewhat broader. For $I < 30°$, the half-width of the profile at $F_{max}/2$ is about equal to the depth. When I is smaller, the depth is roughly equal to half the horizontal distance between F_{max} and F_{min}.

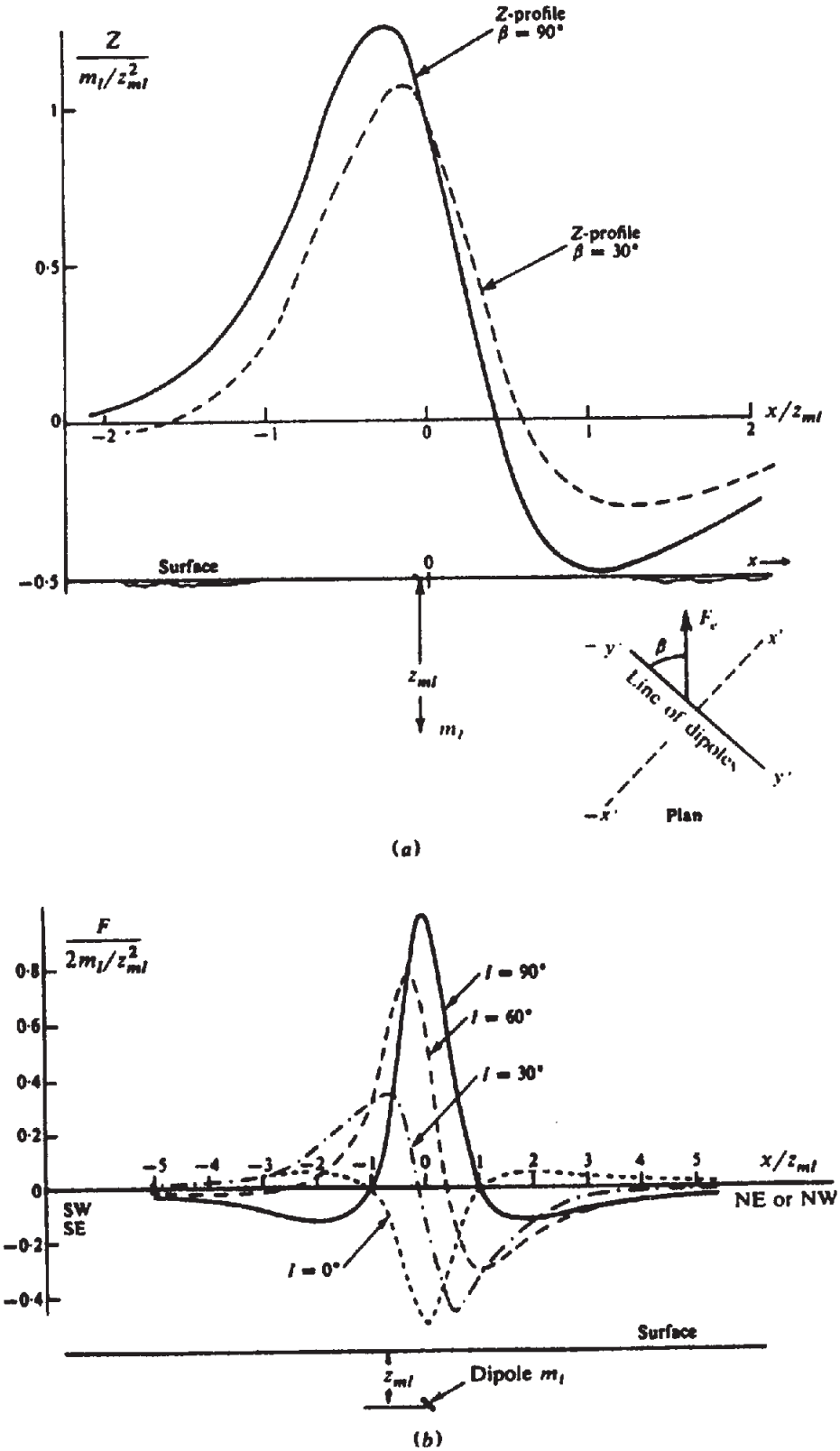

Figure 3.17. Profiles normal to a horizontal line of dipoles. (a) Vertical-field profiles, $I = 45°$. (b) F profiles for $\beta = \pm 45°$.

(c) Line of dipoles (ribbon). The opposite extreme to a line of poles is a magnetic stringer of limited depth extent, which can be modeled by a line (ribbon) of dipoles, sometimes called a thin horizontal cylinder. We take the y' axis along the strike and derive the magnetic response along the principal profile (in the i′ direction) using Poisson's relation [Eq. (3.26)]:

$$A = (m_l/\gamma\rho_l)\, g_a = -(m_l/\gamma\rho_l)\, \nabla U \cdot \alpha_1$$

where ρ_l is the density per unit length and m_l is the dipole moment per unit length in the direction $\alpha_1 = \cos I \sin\beta \mathbf{i}' + \sin I \mathbf{k}$. Then $U = -2\gamma\rho_l \ln(r)$ for infinitesimal cross section [Eq. (2.8)]; we now write $r^2 = x'^2 + (z_{ml} - z)^2$, differentiate, then set $z = 0$. This gives

$$\nabla U = -2\gamma\rho_l (x'\mathbf{i} - z_{ml}\mathbf{k})/r^2$$

The magnetic potential becomes

$$\begin{aligned} A &= \{(-m_l/\gamma\rho_l)(-2\gamma\rho_l)(x'\mathbf{i}' - z_{ml}\mathbf{k})/r^2\} \cdot \alpha_1 \\ &= (2m_l/r^2)(x'\mathbf{i}' - z_{ml}\mathbf{k}) \\ &\quad \cdot (\cos I \sin\beta \mathbf{i}' + \sin I \mathbf{k}) \\ &= (2m_l/r^2)(x' \cos I \sin\beta - z_{ml} \sin I) \end{aligned}$$

The field components are found from this (noting that H is along the x' axis so that the component along the x axis is $H \sin\beta$ – see Eq. (3.41c))

$$\begin{aligned} Z &= -\partial A/\partial z \\ &= (2m_l/r^4) \\ &\quad \times \{(z_{ml}^2 - x'^2)\sin I - 2x'z_{ml} \cos I \sin\beta\} \end{aligned} \tag{3.41a}$$

$$\begin{aligned} H &= -\partial A/\partial x' \\ &= (2m_l/r^4) \\ &\quad \times \{(x'^2 - z_{ml}^2)\cos I \sin\beta - 2x'z_{ml} \sin I\} \end{aligned} \tag{3.41b}$$

$$\begin{aligned} F &= (H \sin\beta)\cos I + Z \sin I \\ &= (2m_l/r^4) \\ &\quad \times \{(x'^2 - z_{ml}^2)(\cos^2 I \sin^2\beta - \sin^2 I) \\ &\qquad - 4x'z_{ml} \sin I \cos I \sin\beta\} \end{aligned} \tag{3.41c}$$

Two principal profiles for the vertical component are shown in Figure 3.17a, one where the dipole line strikes E–W ($\beta = \pi/2$) and one for a strike N30°W ($\beta = \pi/6$). When the dipole line is in the magnetic meridian, $\beta = 0$, the curve is symmetrical with Z_{max} directly above the center. As in the case of the dipole, the depth to the center of the dipole line is approximately equal to the width of the profile at $Z_{max}/2$.

Figure 3.17b displays total-field principal profiles for a line of dipoles striking NW (or NE) for inclinations $I = 90°, 60°, 30°, 0°$. When $0° \le I \le 15°$ and $45° \le I \le 90°$, the full width of $F_{max}/2$ is roughly the depth, whereas for $15° \le I \le 45°$, the depth is approximately the distance between F_{max} and F_{min}. These profiles are also more diagnostic of dip than Z measurements are.

3.6.5. Dipping Dike (Prism)

(a) General case. Magnetic anomalies caused by intrusions, flows, or iron-rich sedimentary horizons are common features in regions favorable for mineral exploration, and there is frequently a contrast in the magnetic mineral content of such features with respect to the host rock. Such features may often be simulated by a two-dimensional dipping dike (prism). A vertical dike is also commonly used in making basement depth determinations in oil prospecting.

Direct application of Poisson's relation is difficult, so we proceed as follows. We assume a dike with dip ξ and strike β, and we take the y' axis along the strike direction. We assume that magnetic polarization is in the $\mathbf{F}_e$ direction, that is, $\mathbf{M} = k\mathbf{F}_e$. The geometry is illustrated in Figure 3.18a, from which we have the following relations:

$$\begin{aligned} r_1^2 &= d^2 + (x + d\cot\xi)^2 \\ r_2^2 &= D^2 + (x + D\cot\xi)^2 \\ r_3^2 &= d^2 + (x + d\cot\xi - b)^2 \\ r_4^2 &= D^2 + (x + D\cot\xi - b)^2 \\ \phi_1 &= \tan^{-1}\{d/(x + d\cot\xi)\} \end{aligned}$$

and so on. Starting with Equation (3.26), we have

$$A = (M/\gamma\rho)\, g_f = -(M/\gamma\rho)\, \nabla U \cdot \mathbf{f}_1 \tag{3.42}$$

where $\mathbf{f}_1 = (\cos I \sin\beta \mathbf{i}' + \sin I \mathbf{k})$. Using Equation (3.27a) this becomes

$$\begin{aligned} \mathbf{F} &= -\nabla A = (M/\gamma\rho)\, \nabla(\nabla U \cdot \mathbf{f}_1) \\ &= (M/\gamma\rho)\, \nabla(U_x \cos I \sin\beta + U_z \sin I) \\ &= (kF_e/\gamma\rho)\{(U_{xx} \cos I \sin\beta + U_{xz} \sin I)\mathbf{i}' \\ &\qquad + (U_{xz} \cos I \sin\beta + U_{zz} \sin I)\mathbf{k}\} \end{aligned} \tag{3.43}$$

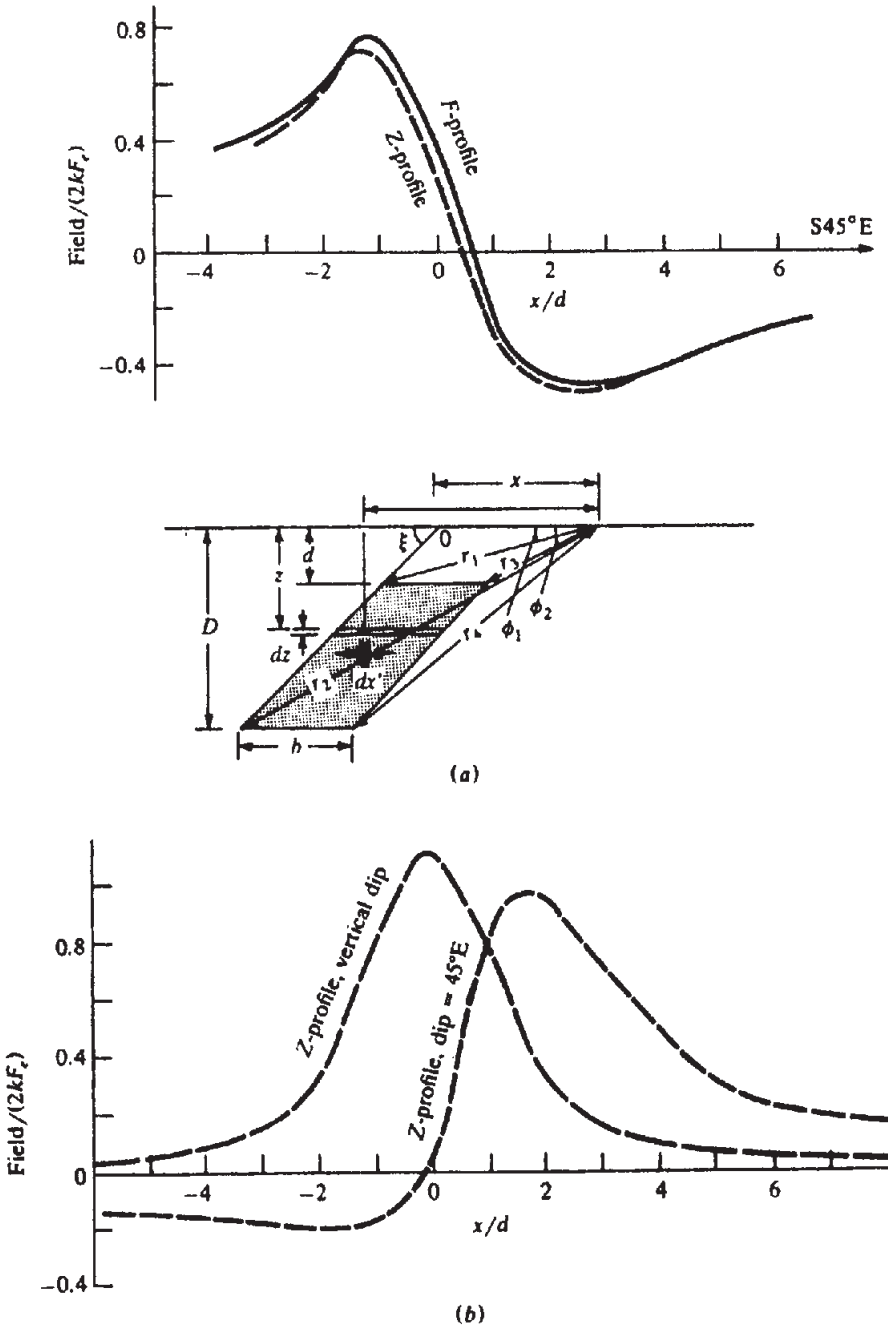

Figure 3.18. Profiles for dike model. L = ∞ except for (d). (a) F, Z profiles for I = 60°, β = 45°, ξ = 45°, b = 2d, D = 3.5d. (b) Z profiles for I = 75°, β = 0°, ξ = 45°E and 90°, b = 2d, D = ∞.

Because U satisfies Laplace's equation (2.11a), $U_{xx} = -U_{zz}$. Differentiating Equation (2.9), we get

$$U_{xz} = 4\gamma\rho \int\int \left(xz/r^4 \right) dx\, dz$$

$$U_{zz} = 2\gamma\rho \int\int \left\{ \left(z^2 - x^2 \right)/r^4 \right\} dx\, dz$$

We change x and z to x' and z', the coordinates of a point inside the dike. r^2 becomes $(x'^2 + z'^2)$. Then,

$$U_{xz} = 4\gamma\rho \int_{x'}\int_{z'} \frac{x'z'}{r^4}\, dx'\, dz'$$

$$= 4\gamma\rho \int z'\, dz' \int \frac{x'\, dx'}{\left(z'^2 + x'^2 \right)^2}$$

$$= 4\gamma\rho \int z'\, dz' \left\{ \frac{-1}{2\left(z'^2 + x'^2 \right)} \right\} \Bigg|_{x + z' \cot \xi}^{x + z' \cot \xi - b}$$

$$= 2\gamma\rho \int_d^D \left\{ \frac{z'}{z'^2 \csc^2 \xi + 2z'x \cot \xi + x^2} - \frac{z'}{z'^2 \csc^2 \xi + 2z'(x - b)\cot \xi + (x - b)^2} \right\} dz'$$

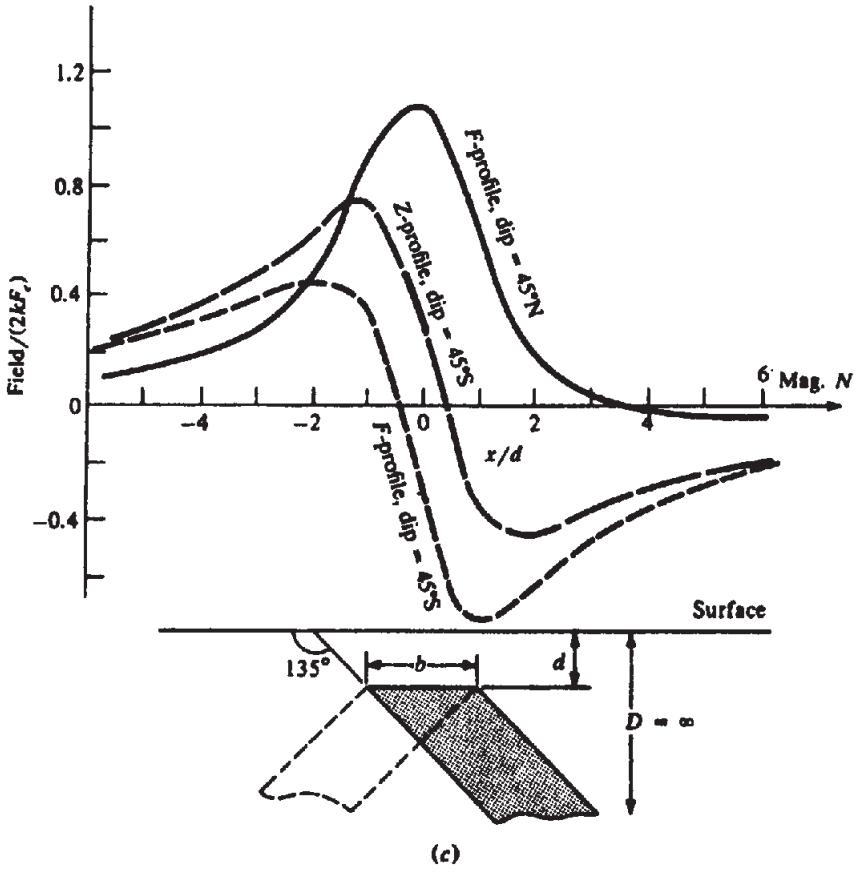

(c)

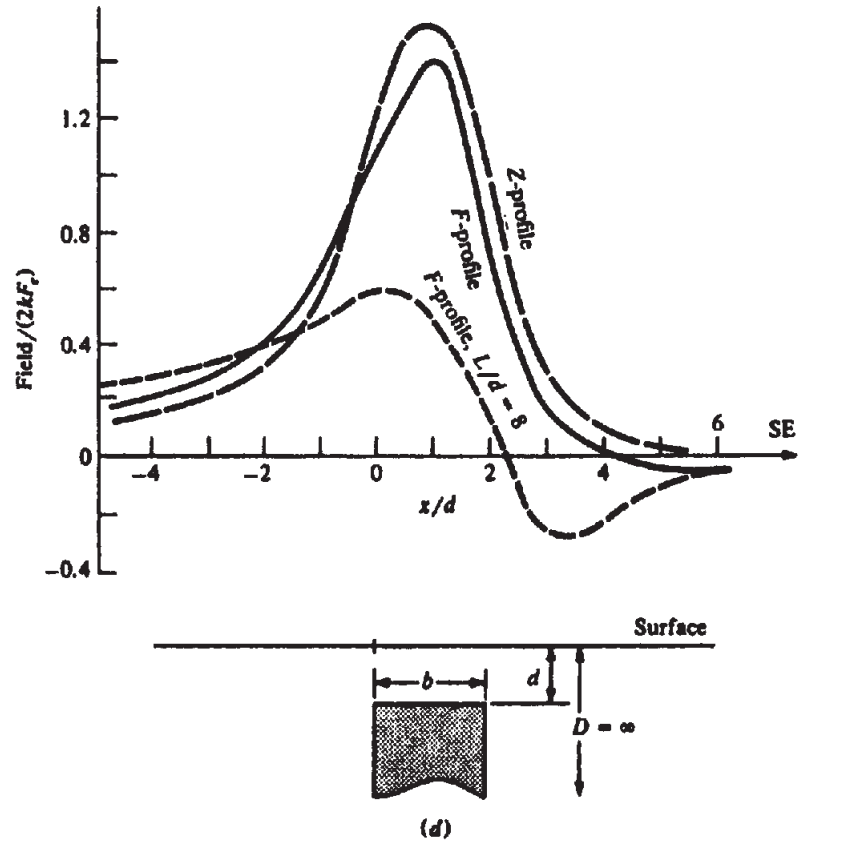

(d)

Figure 3.18. (Continued) (c) F, Z profiles for I = 60°, β = 90°, ξ = 45°N and S, b = 2d, D = ∞. (d) F, Z profiles for I = 75°, β = 90°, ξ = 90°, b = 2d, D = ∞, 2L = ∞ and 16d.

After some manipulation, this becomes

$$U_{xz} = 2\gamma\rho \sin\xi\{\sin\xi \ln(r_2r_3/r_1r_4) + \cos\xi(\phi_1 - \phi_2 - \phi_3 + \phi_4)\}$$

The value of U_{zz} can be found the same way; the result is

$$U_{zz} = 2\gamma\rho \sin\xi\{\cos\xi \ln(r_2r_3/r_1r_4) - \sin\xi(\phi_1 - \phi_2 - \phi_3 + \phi_4)\}$$

Substitution of the values of the derivatives in Equation (3.43) gives

$$Z = 2kF_e \sin\xi\{(\cos I \sin\xi \sin\beta + \sin I \cos\xi)\ln(r_2r_3/r_4r_1) + (\cos I \cos\xi \sin\beta - \sin I \sin\xi) \times(\phi_1 - \phi_2 - \phi_3 + \phi_4)\} \quad (3.44a)$$

$$H = 2kF_e \sin\xi \sin\beta \times\{(\sin I \sin\xi - \cos I \cos\xi \sin\beta)\ln(r_2r_3/r_4r_1) + (\cos I \sin\xi \sin\beta + \sin I \cos\xi) \times(\phi_1 - \phi_2 - \phi_3 + \phi_4)\} \quad (3.44b)$$

$$F = 2kF_e \sin\xi\Big[\{\sin 2I \sin\xi \sin\beta - \cos\xi(\cos^2 I \sin^2\beta - \sin^2 I)\} \times\ln(r_2r_3/r_4r_1) + \{\sin 2I \cos\xi \sin\beta + \sin\xi(\cos^2 I \sin^2\beta - \sin^2 I)\} \times(\phi_1 - \phi_2 - \phi_3 + \phi_4)\Big] \quad (3.44c)$$

The parameter values in these equations may sometimes be found from the interpretation of ground surveys, but generally this cannot be done for airborne work. Monopole- and dipole-line approximations (§3.6.4b, c) may occasionally be distinguished from dike-like models of considerable width in mineral exploration, but usually basement is so far removed from the aircraft in oil reconnaissance work that discrimination is impossible. The vertical dike is often used for basement depth determinations in the latter case.

(b) E–W or N–S strike. When the dike strikes E–W, $\beta = 90°$ and Equations (3.44a, c) become

$$Z = 2kF_e \sin\xi\{\sin(I + \xi)\ln(r_2r_3/r_4r_1) + \cos(I + \xi)(\phi_1 - \phi_2 - \phi_3 + \phi_4)\} \quad (3.45a)$$

$$F = 2kF_e \sin\xi\{-\cos(\xi + 2I)\ln(r_2r_3/r_4r_1) + \sin(\xi + 2I) \times(\phi_1 - \phi_2 - \phi_3 + \phi_4)\} \quad (3.45b)$$

If, in addition, the dike has vertical sides, $\xi = 90°$ and Equations (3.45) are simplified to

$$Z = 2kF_e\{\cos I \ln(r_2r_3/r_4r_1) - \sin I(\phi_1 - \phi_2 - \phi_3 + \phi_4)\} \quad (3.46a)$$

$$F = 2kF_e\{\sin 2I \ln(r_2r_3/r_4r_1) + \cos 2I(\phi_1 - \phi_2 - \phi_3 + \phi_4)\} \quad (3.46b)$$

For N–S strike, $\beta = 0$, so

$$Z = 2kF_e \sin\xi \sin I\{\cos\xi \ln(r_2r_3/r_4r_1) - \sin\xi(\phi_1 - \phi_2 - \phi_3 + \phi_4)\} \quad (3.47a)$$

$$F = 2kF_e \sin\xi \sin^2 I\{(\cos\xi)\ln(r_2r_3/r_4r_1) - \sin\xi(\phi_1 - \phi_2 - \phi_3 + \phi_4)\} \quad (3.47b)$$

For a vertical dike with N–S strike, Equations (3.47) become

$$Z = -2kF_e \sin I(\phi_1 - \phi_2 - \phi_3 + \phi_4) \quad (3.48a)$$

$$F = -2kF_e \sin^2 I(\phi_1 - \phi_2 - \phi_3 + \phi_4)\} \quad (3.48b)$$

(c) Dike of limited length. Dike anomalies rarely satisfy the criteria for two-dimensionality (strike length $\geq 10b$, where b is width). For a more realistic model (sometimes called a prism model) having a strike length $2L$, $D = \infty$, and $\xi = 90°$, equation (3.44c) becomes

$$F = kF_e\Bigg\{\sin 2I \sin\beta\Big[\ln\Big\{\left(r_1^2 + L^2\right)^{1/2} + L\Big\} - \ln\Big\{\left(r_1^2 + L^2\right)^{1/2} - L\Big\} + \ln\Big\{\left(r_3^2 + L^2\right)^{1/2} - L\Big\} - \ln\Big\{\left(r_3^2 + L^2\right)^{1/2} + L\Big\}\Big] - (\cos^2 I \sin\beta - \sin^2 I) \times\Bigg[\tan^{-1}\left(\frac{L}{x}\right) - \tan^{-1}\left(\frac{L}{x - b}\right) - \tan^{-1}\left\{\frac{Ld}{x\left(r_1^2 + L^2\right)^{1/2}}\right\} + \tan^{-1}\left\{\frac{Ld}{(x - b)\left(r_3^2 + L^2\right)^{1/2}}\right\}\Bigg]\Bigg\} \quad (3.49)$$

(d) Discussion of principal profiles. Principal profiles are shown in Figure 3.18. In Figure 3.18a, the

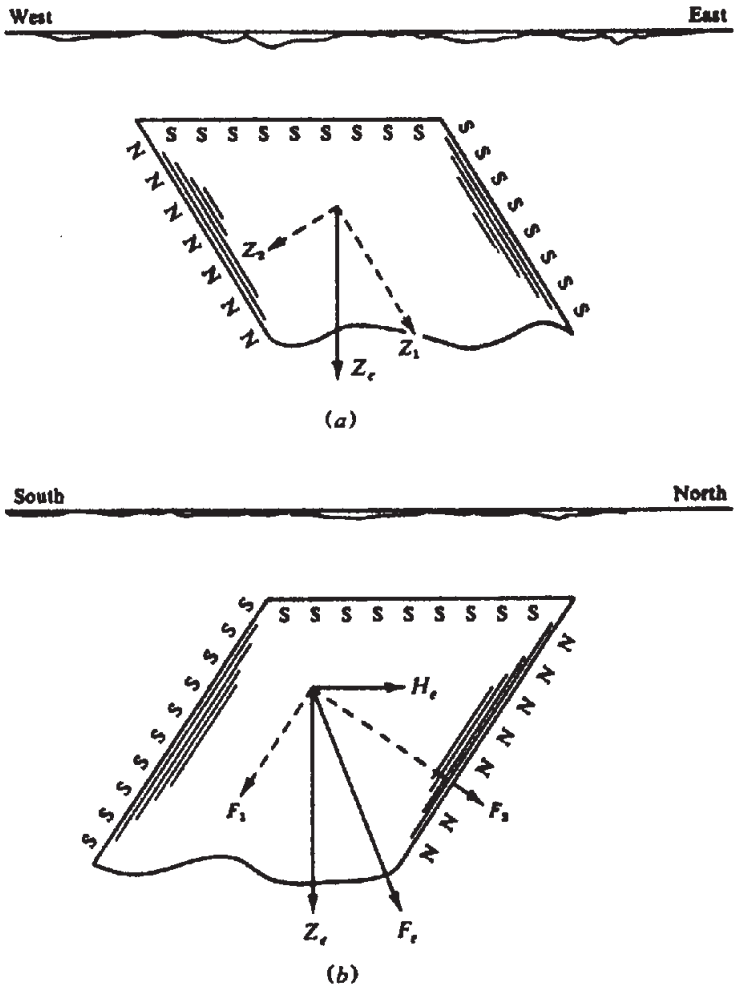

Figure 3.19. Pole distribution in a dike.

dike strikes NE–SW and dips 45°SE. In high magnetic latitudes where the H component is small, strike direction is relatively unimportant. This is clear from Equations (3.44a, c) where, if $I \approx 90°$, the expressions for Z and F are practically independent of the strike direction β.

Figure 3.18b displays profiles for N–S strike. Figure 3.18c is for E–W strike. The asymmetry is less pronounced for north dips than for south dips. In high latitudes a dike with E–W strike and dip I gives a symmetrical Z profile and a nearly symmetrical F profile.

Figure 3.18d is for a vertical dike with NW or NE strike; Z and F profiles for $L = \infty$ are similar because the vertical component of F predominates. Gay (1967) takes advantage of these similarities and obtains a single family of curves for F, Z, and H over the whole range of dips and inclinations, defined by an index response parameter.

Figure 3.18d also shows the total field response over a short dike. The shape is similar to the other two curves but with lower amplitude. This profile is across the center of the dike and normal to the strike.

It is useful to provide a qualitative explanation for the character of the profiles in Figure 3.18 based on pole distribution where the magnetization is mainly induced by the Earth's field. For a dike dipping east and striking N–S as in Figure 3.19a, Z_e will produce N and S poles along the footwall and hanging wall, respectively, as can be seen by resolving Z_e into components parallel and normal to the dip. A similar explanation (Fig. 3.19b) accounts for the more pronounced asymmetry in the profile of the E–W dike dipping south in Figure 3.18c; the N poles on the footwall are produced by components of both H_e and Z_e. In fact, such a dike tends to be magnetized transversely because $\mathbf{F}_e$ is practically normal to the dip axis.

Depth estimates based on width of profiles are not particularly useful unless the profiles are symmetrical and the width is no greater than the depth to the top face. Under these restrictions the rule for half-width at half-maximum gives the depth to within 20%, that is, $x_{1/2} \approx d$ at $Z = Z_{max}/2$. Several techniques based on profile slopes are effective for depth determination for the dike model (§3.7.11b). Direction of dip is usually fairly obvious from the profiles

since we know the total-field direction. The situation is complicated, however, because we cannot determine in advance the presence and direction of remanent magnetism and we have difficulty in determining the zero line for a field profile, that is, in isolating a single anomaly. A solution to finding the zero line for the dike model is given in Section 3.7.8.

The dike profiles in Figure 3.18b, c, and d were simplified by assuming infinite depth extent ($D = \infty$). They are not greatly changed for finite depth extent unless the depth extent is less than five times the width of the top face, in which case the positive tails are pulled down slightly. For very shallow dip, short strike length, and small depth extent (effectively a flat-lying plate magnetized transversely), the profiles becomes more symmetrical, with a broad maximum of small magnitude above the plate and negative tails at the flanks.

3.6.6. Dipping Sheet

The expressions for Z and F profiles over a thin sheet may be derived from Equation (3.44) by replacing the horizontal width b of the dipping dike model with $t \csc \xi$, where t is the thickness of the sheet. The principal reason for considering the thin sheet is that the expressions are simpler than for the dike and are sufficiently accurate provided the thickness t is not greater than the depth to the top d. The thin sheet geometry is also common in mineral exploration areas.

For the geometry shown in Figure 3.20a, the result is

$$Z = 2ktF_e\big[(1/r_2)\{\cos I \sin\beta \sin(\xi+\theta_2) + \sin I \cos(\xi+\theta_2)\} - (1/r_1)\{\cos I \sin\beta \sin(\xi+\theta_1) + \sin I \cos(\xi+\theta_1)\}\big] \quad (3.50a)$$

$$F = 2ktF_e\big[(1/r_2)\{\sin 2I \sin\beta \sin(\xi+\theta_2) - (\cos^2 I \sin^2\beta - \sin^2 I) \times \cos(\xi+\theta_2)\} - (1/r_1)\{\sin 2I \sin\beta \sin(\xi+\theta_1) - (\cos^2 I \sin^2\beta - \sin^2 I) \times \cos(\xi+\theta_1)\}\big] \quad (3.50b)$$

When the strike is E–W ($\beta = 90°$), Equations (3.50) become

$$Z = 2ktF_e\{\sin(\xi + I + \theta_2)/r_2 - \sin(\xi + I + \theta_1)/r_1\} \quad (3.51a)$$

$$F = -2ktF_e\{\cos(\xi + 2I + \theta_2)/r_2 - \cos(\xi + 2I + \theta_1)/r_1\} \quad (3.51b)$$

and when the strike is N–S ($\beta = 0°$),

$$Z = 2ktF_e \sin I\{\cos(\xi+\theta_2)/r_2 - \cos(\xi+\theta_1)/r_1\} \quad (3.52a)$$

$$F = 2ktF_e \sin^2 I\{\cos(\xi+\theta_2)/r_2 - \cos(\xi+\theta_1)/r_1\} \quad (3.52b)$$

If the sheet is vertical, $\xi = 90°$ and Equations (3.50b), (3.51b), and (3.52b) simplify to

$$F = 2ktF_e\big[(1/r_2)\{\sin 2I \sin\beta \cos\theta_2 + (\cos^2 I \sin^2\beta - \sin^2 I)\sin\theta_2\} - (1/r_1)\{\sin 2I \sin\beta \cos\theta_1 + (\cos^2 I \sin^2\beta - \sin^2 I)\sin\theta_1\}\big] \quad (3.53a)$$

$$F = 2ktF_e\{\sin(2I+\theta_2)/r_2 - \sin(2I+\theta_1)/r_1\} \quad (3.53b)$$

$$F = -2ktF_e \sin^2 I(\sin\theta_2/r_2 - \sin\theta_1/r_1) \quad (3.53c)$$

The profiles in Figure 3.20 for $I = 60°$ are similar to, although sharper than, those for the dike. Rough dip estimates are possible when the strike of the body and total-field direction are known. Depth estimates from curve widths are fairly good when the curves are roughly symmetrical, but not practical when the sheet extends to great depth. The half-widths at $Z_{max}/2$ for the short vertical and dipping models give $x_{1/2} \approx 1.7d$.

When the depth extent is very great, $r_2 \approx \infty$ and the sheet is effectively a half-plane. Then for Z and F we have from Equations (3.50),

$$Z = -(2ktF_e/r_1)\{\cos I \sin\beta \sin(\xi+\theta_1) + \sin I \cos(\xi+\theta_1)\} \quad (3.54a)$$

$$F = -(2ktF_e/r_1)\{\sin 2I \sin\beta \sin(\xi+\theta_1) - (\cos^2 I \sin^2\beta - \sin^2 I)\cos(\xi+\theta_1)\} \quad (3.54b)$$

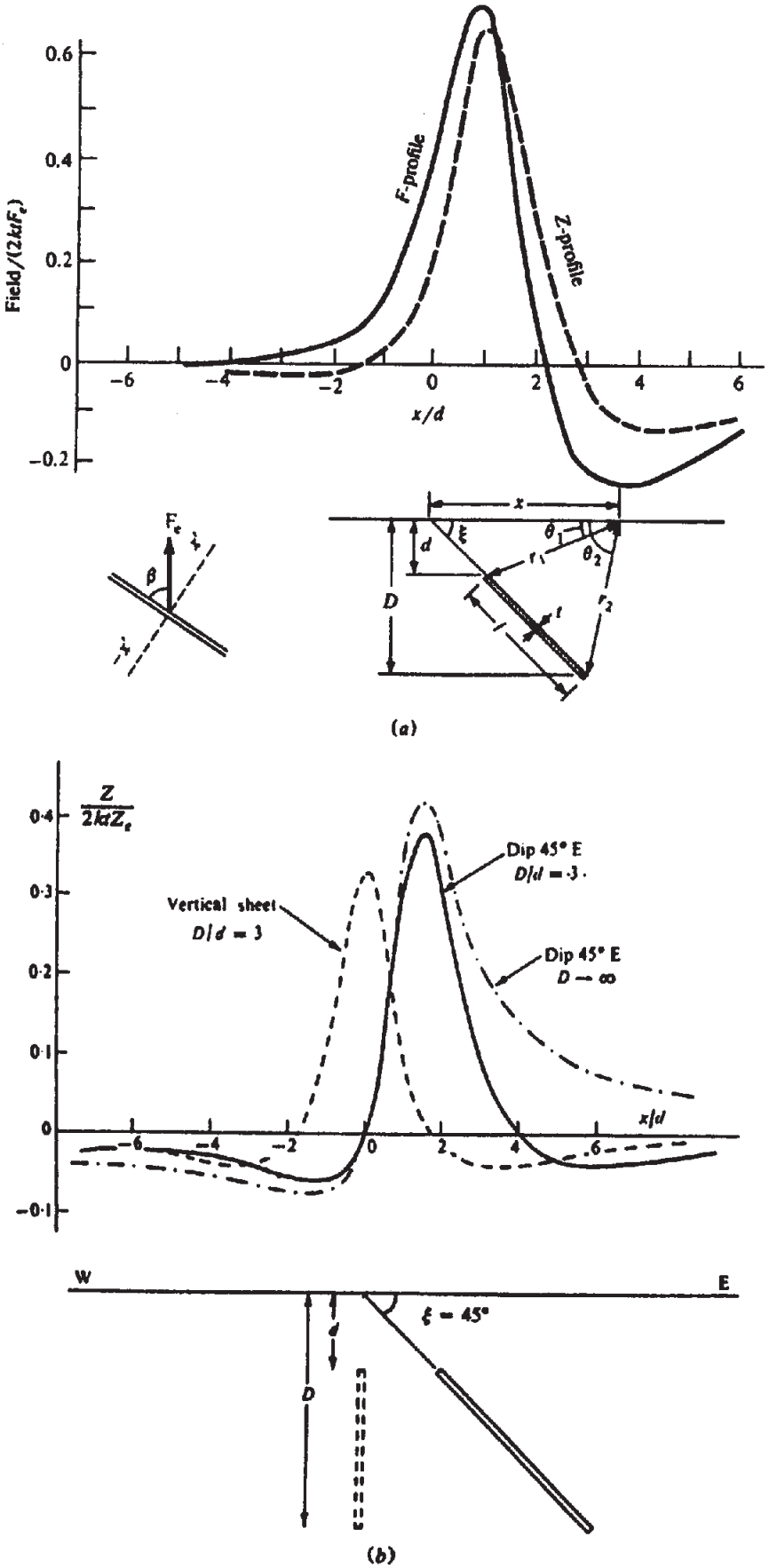

Figure 3.20. Thin sheet; I = 60°, D/d = 3. (a) F, Z profiles for ξ = 45°NE, β = 60°. (b) Z profiles for N–S strike (β = 0°), ξ = 45°N and 90°, and effect of depth extent.

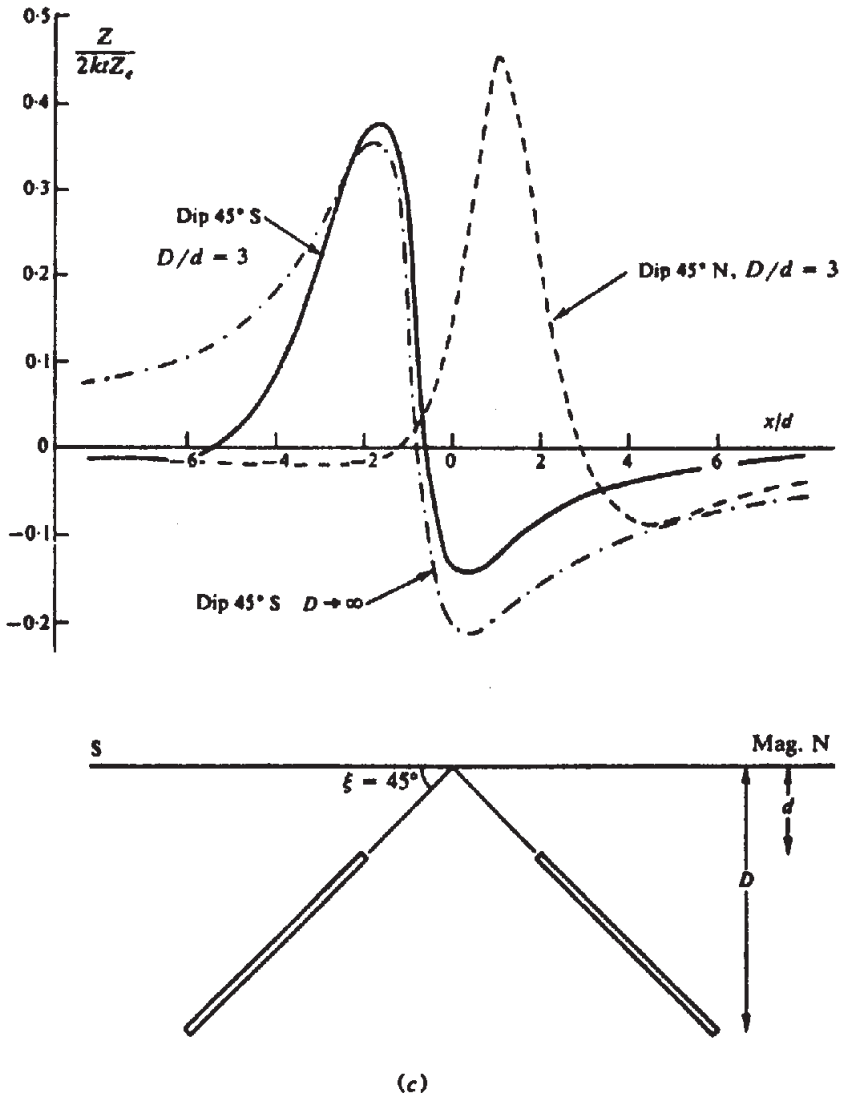

(c)

Figure 3.20. (Continued) (c) Z profiles for E–W strike, $\xi = 45°$N and 45°S, $\beta = 90°$.

For this limiting case we can determine the depth and dip uniquely. Setting $dZ/dx = dF/dx = 0$, we obtain the x values for the maximum and minimum values for Z and F. This yields the following relations for Z:

$$x_m/d = 2\left(\cos^2 I \sin^2\beta + \sin^2 I\right)^{1/2} / \left(\cos I \sin\beta \sin\xi + \sin I \cos\xi\right) \quad (3.55a)$$

$$x_{1/2}/d = \left\{\cos^2 I \sin^2\beta + \sin^2 I\right\}^{1/2} / \left(\cos I \sin\beta \cos\xi + \sin I \sin\xi\right) \quad (3.55b)$$

where $x_m = x_{max} - x_{min}$ and $x_{1/2}$ is the full width at half-maximum. Likewise, writing x'_m, $x'_{1/2}$ for the F curve, we have

$$x'_m/d = 2\left\{\sin^2 2I \sin^2\beta + \left(\sin^2 I - \cos^2 I \sin^2\beta\right)^2\right\}^{1/2} / \left\{\sin 2I \sin\beta \sin\xi + \left(\sin^2 I - \cos^2 I \sin^2\beta\right)\cos\xi\right\} \quad (3.56a)$$

$$x'_{1/2}/d = \left\{\sin^2 2I \sin^2\beta + \left(\sin^2 I - \cos^2 I \sin^2\beta\right)^2\right\}^{1/2} / \left\{\sin 2I \sin\beta \cos\xi + \left(\sin^2 I - \cos^2 I \sin^2\beta\right)\sin\xi\right\} \quad (3.56b)$$

Combining Equations (3.55), we obtain the dip

angle ξ,

$$\tan\xi = \left(-2x_{1/2}\cos I\sin\beta + x_m\sin I\right) / \left(2x_{1/2}\sin I - x_m\cos I\sin\beta\right) \quad (3.57a)$$

and the depth,

$$d = x_m x_{1/2} / \left(x_m^2 + 2x_{1/2}^2\right)^{1/2} \quad (3.57b)$$

When the sheet is not two dimensional, we can modify Equations (3.50) for a length $2L$. Then the principal profiles for Z and F become

$$Z = 2ktLF_e\{(Q+R)\cos I\sin\beta + (S+T)\sin I\} \quad (3.58a)$$

$$F = 2ktLF_e\{(Q+R)\sin 2I\sin\beta) - (S+T)(\cos^2 I\sin^2\beta - \sin^2 I)\} \quad (3.58b)$$

where

$$\left.\begin{aligned} Q &= \sin(\xi+\theta_2)/\left\{r_2\left(r_2^2+L^2\right)^{1/2}\right\} \\ &\quad - \sin(\xi+\theta_1)/\left\{r_1\left(r_1^2+L^2\right)^{1/2}\right\} \\ R &= \left\{x\sin^2\xi\cos\xi/\left(x^2\sin^2\xi+L^2\right)\right\} \\ &\quad \times\left\{\cot(\xi-\theta_2)/\left(r_2^2+L^2\right)^{1/2} \right. \\ &\quad \left. -\cot(\xi-\theta_1)/\left(r_1^2+L^2\right)^{1/2}\right\} \\ S &= \cos(\xi+\theta_2)/\left\{r_2\left(r_2^2+L^2\right)^{1/2}\right\} \\ &\quad - \cos(\xi+\theta_1)/\left\{r_1\left(r_1^2+L^2\right)^{1/2}\right. \\ T &= \left\{x\cos^2\xi\sin\xi/\left(x^2\sin^2\xi+L^2\right)\right\} \\ &\quad \times\left\{\cot(\xi-\theta_2)/\left(r_2^2+L^2\right)^{1/2} \right. \\ &\quad \left. -\cot(\xi-\theta_1)/\left(r_1^2+L^2\right)^{1/2}\right\} \end{aligned}\right\} \quad (3.58c)$$

The profile is reduced in magnitude but otherwise unchanged in shape.

3.6.7. Horizontal Sheet (Plate)

When the sheet is horizontal (see Fig. 3.21a), $\xi = 0$, d becomes the depth of the sheet, and Equations (3.50) give

$$Z = -2ktF_e\left[(1/r_1)(\cos I\sin\beta\sin\theta_1 + \sin I\cos\theta_1) - (1/r_2)(\cos I\sin\beta\sin\theta_2 + \sin I\cos\theta_2)\right]$$

$$F = -2ktF_e\left[(1/r_1)\{\sin 2I\sin\beta\sin\theta_1 - (\cos^2 I\sin^2\beta - \sin^2 I)\cos\theta_1\} - (1/r_2)\{\sin 2I\sin\beta\sin\theta_2 - (\cos^2 I\sin^2\beta - \sin^2 I)\cos\theta_2\}\right]$$

where $r_1^2 = x^2 + d^2$, $r_2^2 = (x-l)^2 + d^2$, $\sin\theta_1 = d/r_1$, $\cos\theta_1 = x/r_1$, $\sin\theta_2 = d/r_2$, and $\cos\theta_2 = (x-l)/r_2$. Eliminating θ_1 and θ_2, we get

$$Z = -2ktF_e\left[(1/r_1)^2(d\cos I\sin\beta + x\sin I) - (1/r_2)^2\{d\cos I\sin\beta + (x-l)\sin I\}\right] \quad (3.59a)$$

$$F = -2ktF_e\left[(1/r_1)^2\{d\sin 2I\sin\beta - x(\cos^2 I\sin^2\beta - \sin^2 I)\} - (1/r_2)^2\{d\sin 2I\sin\beta - (x-l) \times(\cos^2 I\sin^2\beta - \sin^2 I)\}\right] \quad (3.59b)$$

Figure 3.21 shows profiles for horizontal plates. In Figure 3.21a, a shallow plate striking north–south produces a symmetrical Z profile. The F profile (not shown) is the same as the Z profile but reduced in magnitude by the multiplier $\sin I$. It is not possible to make good depth estimates from the width of these curves, but other techniques are available (see §3.7.8 and §3.7.11).

Over a horizontal thin sheet of finite strike length $2L$, Equation (3.59b) becomes

$$F = -2ktF_e\left[\{d\sin 2I\sin\beta - x(\cos^2 I\sin^2\beta - \sin^2 I)\} / r_1\left(1 + r_1^2/L^2\right)^{1/2} - \{d\sin 2I\sin\beta - (x-l) \times(\cos^2 I\sin^2\beta - \sin^2 I)\} / r_2\left(1 + r_2^2/L^2\right)^{1/2}\right] \quad (3.60)$$

Total-field profiles for the thin plate, illustrated in Figure 3.21b for infinite strike length and for $2L = 4l$, are remarkably similar. (This is also true for gravity profiles over a thin plate.) Unless $L < l$, the finite length does not affect the curve more than 20%.

Use of both the bottomless dike and the thin sheet models yields minimum and maximum depths, respectively, for d. Sharpness of the peak is characteristic of a shallow plate compared with the dike.

3.6.8. Semiinfinite Horizontal Sheet: Fault Approximation

If r_2 (or r_1) approaches infinity, l becomes very large and Equations (3.59) reduce to one term for a semiinfinite sheet. Profiles for vertical component and total field are illustrated in Figure 3.22. In Figure 3.22a, the strike is N–S with $I = 60°$; both curves

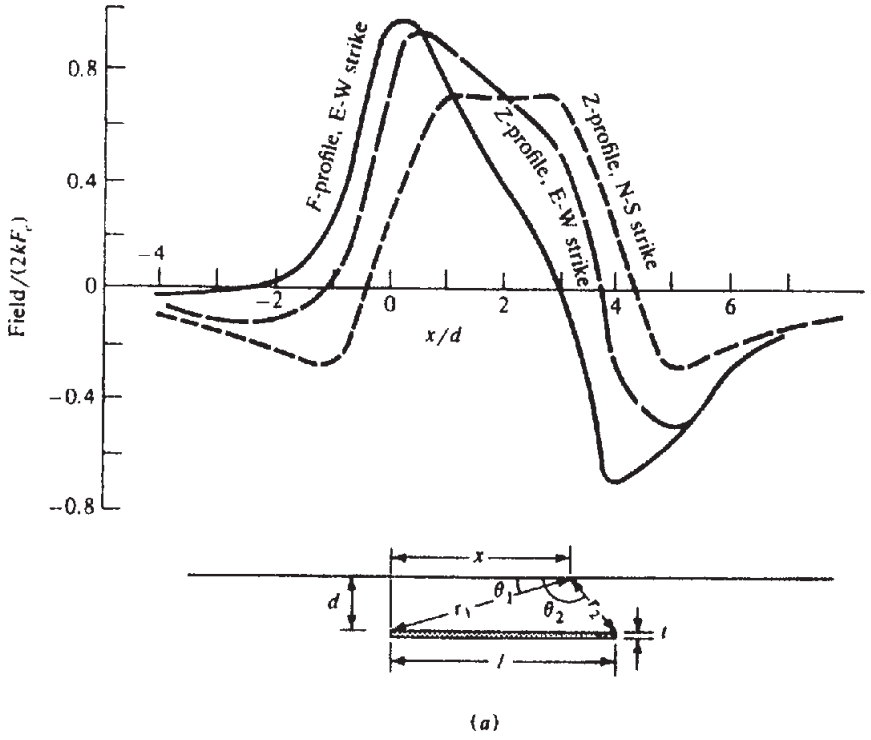

Figure 3.21. Thin horizontal plate of finite width, $t/l = 0.125$. (a) Profiles for $I = 60°$, $\beta = 0°$ and $90°$, $d/l = 0.25$.

are antisymmetrical. The response in Figure 3.22b is similar to those from targets with steep dip. Both E–W profiles provide good depth estimates; d equals half the horizontal distance between Z_{max} and Z_{min} (or F_{max} and F_{min}). This measurement is 25% too large for the N–S profile (Fig. 3.22a).

It is necessary to traverse a considerable distance before the magnetic background is reached. For example, when $d = 30$ m, the survey should extend at least 800 m either way from the edge of the sheet. In practical situations this often cannot be done because there are likely to be other magnetic features in the vicinity.

If we introduce another semiinfinite sheet at a different depth, as shown in Figure 3.23, we have an approximation to a fault. When the fault plane has dip ξ, Equations (3.59) give

$$\begin{aligned} Z = -2ktF_e\big[&(1/r_1^2)\{\, d\cos I\sin\beta \\ &+(x + d\cot\xi)\sin I\,\} \\ &-(1/r_2^2)\{\, D\cos I\sin\beta \\ &+(x + D\cot\xi)\sin I\,\}\big] \end{aligned} \tag{3.61a}$$

$$\begin{aligned} F = -2ktF_e\big[&(1/r_1^2)\{\, d\sin 2I\sin\beta \\ &-(x + d\cot\xi)(\cos^2 I\sin^2\beta - \sin^2 I)\,\} \\ &-(1/r_2^2)\{\, D\sin 2I\sin\beta \\ &-(x + D\cot\xi)(\cos^2 I\sin^2\beta - \sin^2 I)\,\}\big] \end{aligned} \tag{3.61b}$$

where

$$r_1^2 = d^2 + (x + d\cot\xi)^2$$

$$r_2^2 = D^2 + (x + D\cot\xi)^2$$

For a vertical fault, Z and F profiles are shown in Figure 3.23a. Responses from normal faults are similar to these examples regardless of strike, but a profile over a reverse fault reflects the concentration of anomalous material in the area of overlap and resembles the response of a steeply dipping target. An estimate of the depth to the upper bed can be made in terms of $x_{1/2}$, half the distance between Z_{max} and Z_{min}: $0.5 \le x_{1/2}/d \le 1.25$. The lower limit applies when the lower bed is only slightly displaced; the upper limit applies when D/d is large. When the fault-plane dip ξ is fairly steep, $\xi \approx 90°$ and D can be estimated from

$$\begin{aligned} D \approx x_{1/2}\big[&Z_m\big(1 + x_{1/2}^2/d^2\big) \\ &/\big\{2x_{1/2}(dZ/dx)_{max} \\ &-Z_m\big(1 + x_{1/2}^2/d^2\big)\big\}, \end{aligned} \tag{3.62}$$

where $Z_m = Z_{max} - Z_{min}$ and $(dZ/dx)_{max}$ is the maximum slope.

The fault approximation in Equations (3.61) is accurate to within a few percent provided d is larger

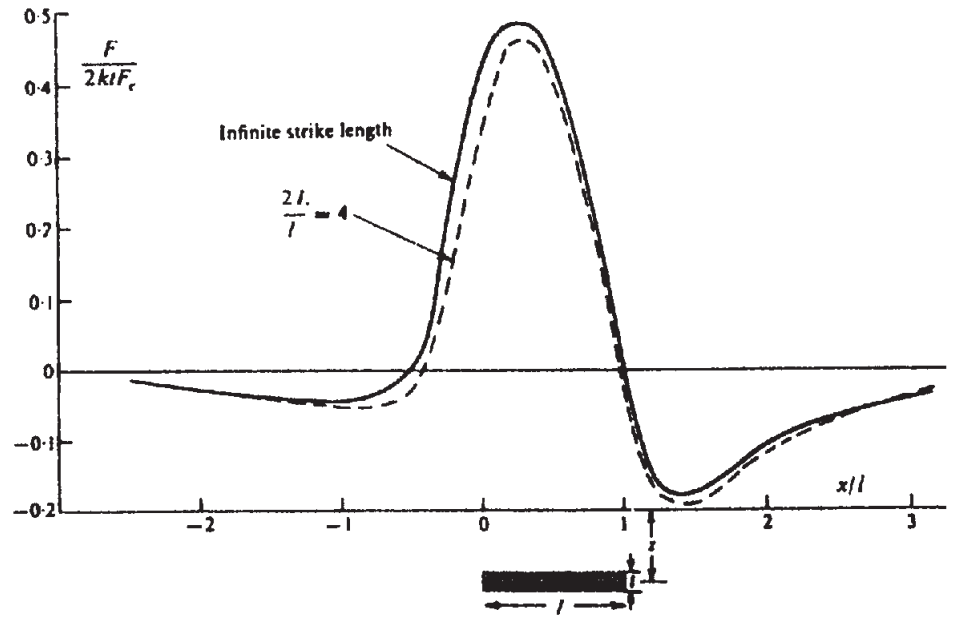

(b)

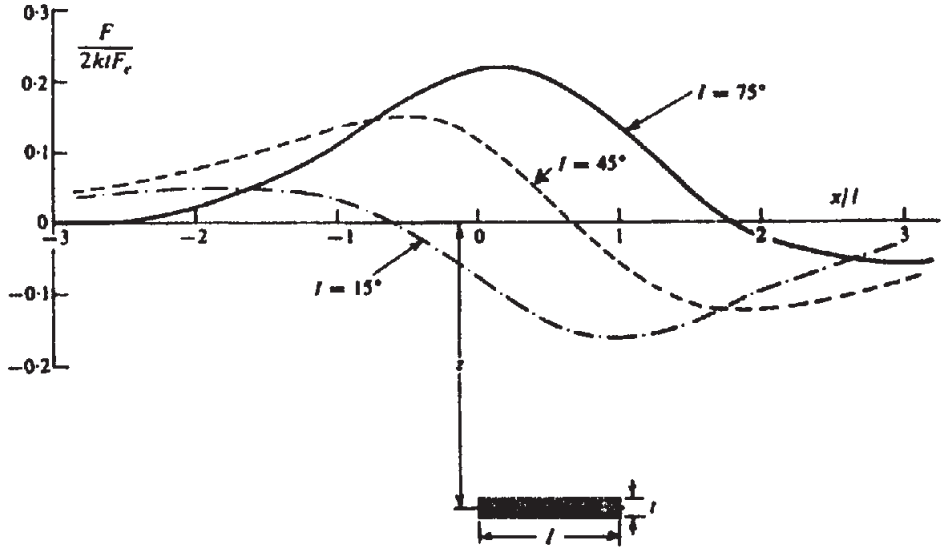

(c)

Figure 3.21. (Continued) (b) Profiles for $l = 75°$, $\beta = 45°$, $d/l = 0.5$. (c) Profiles for $l = 15°$, $\beta = 45°$, $d/l = 2$.

than $2t$. When this assumption is not valid, it is necessary to use the dike model (§3.6.5). With $r_3 = r_4 = \infty$ and $\phi_3 = \phi_4 = \pi$, the Z and F expressions for the horizontal slab are identical to Equations (3.44) to (3.48) with the terms in r_3, r_4, ϕ_3, and ϕ_4 omitted (see Fig. 3.24). Figure 3.24 shows F profiles over a single horizontal bed with N–S strike and face angles of 45° and 135°. The curves are reflections of each other in both axes.

To simulate a fault, we add a similar slab at a different depth (as in Fig. 2.32), for example, for E–W strike and strike length $2L$, we get

$$Z = 2kF_e \sin\xi[Q \ln(r_2 r_7 / r_1 r_8) + R(\phi_1 - \phi_2 - \phi_7 + \phi_8)] \quad (3.63a)$$

$$F = 2kF_e \sin\xi[S \ln(r_2 r_7 / r_1 r_8) + T(\phi_1 - \phi_2 - \phi_7 + \phi_8)] \quad (3.63b)$$

where Q, R, S, and T are as in Equations (3.58c). [Note that ξ in Eqs. (3.63) and in the factors Q, R, S, and T is the slope of the fault plane.]

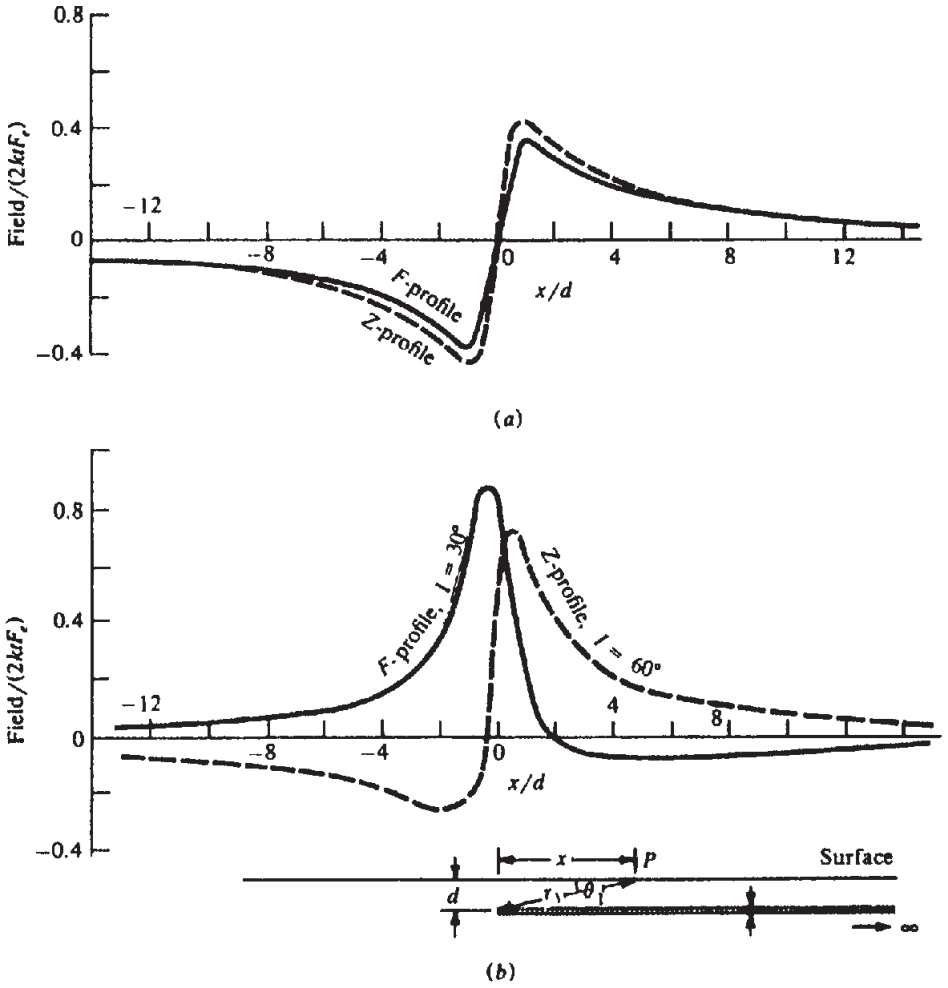

Figure 3.22. Semiinfinite horizontal sheet. F, Z profiles for (a) N–S strike, I = 60°; (b) E–W strike, I = 60 and 30°.

3.6.9. Contact between Beds of Different Susceptibilities

A common magnetic structure results from the contact of two slabs with contrasting susceptibility values (see Fig. 3.25). Because a uniform continuous slab creates no magnetic anomaly, the effect of the contact is the same as that of the semiinfinite slab to the left with susceptibility $\Delta k = k' - k$. From Equation (3.44), we have

$$Z = 2\,\Delta k\,F_e \sin\xi\{(\cos I \sin\xi \sin\beta + \sin I \cos\xi)\ln(r_2/r_1) + (\cos I \cos\xi \sin\beta - \sin I \sin\xi)(\phi_1 - \phi_2)\} \quad (3.64a)$$

$$F = 2\,\Delta k\,F_e\big[\sin\xi\{\sin 2I \sin\xi \sin\beta - \cos\xi(\cos^2 I \sin^2\beta - \sin^2 I)\}\ln(r_2/r_1) + \{\sin 2I \cos\xi \sin\beta + \sin\xi(\cos^2 I \sin^2\beta - \sin^2 I)\}(\phi_1 - \phi_2)\big] \quad (3.64b)$$

Figure 3.25 shows profiles over vertical and dipping contacts of considerable depth extent. When $\phi_2 = \pi/2$, Equation (3.64b) becomes, for a vertical contact striking N–S

$$F = 2\,\Delta k\,F_e \sin^2 I\{\pi/2 - \tan^{-1}(d/x)\}$$

$$= 2\,\Delta k\,F_e \sin^2 I \tan^{-1}(x/d) \quad (3.65)$$

The difference between the limiting value of F at $x = \pm\infty$ is

$$\Delta F = F_{max} - F_{min} = 2\pi\,\Delta k\,F_e \sin^2 I$$

The maximum slope occurs over the contact and is given by $(dF/dx)_{x=0} = 2\,\Delta k\,F_e \sin^2 I/d$. We can calculate the susceptibility contrast and depth of the bed:

$$\Delta k = \Delta F \sin^2 I/2\pi F_e \quad \text{and} \quad d = \Delta F/\pi(dF/dx)_{x=0} \quad (3.66)$$

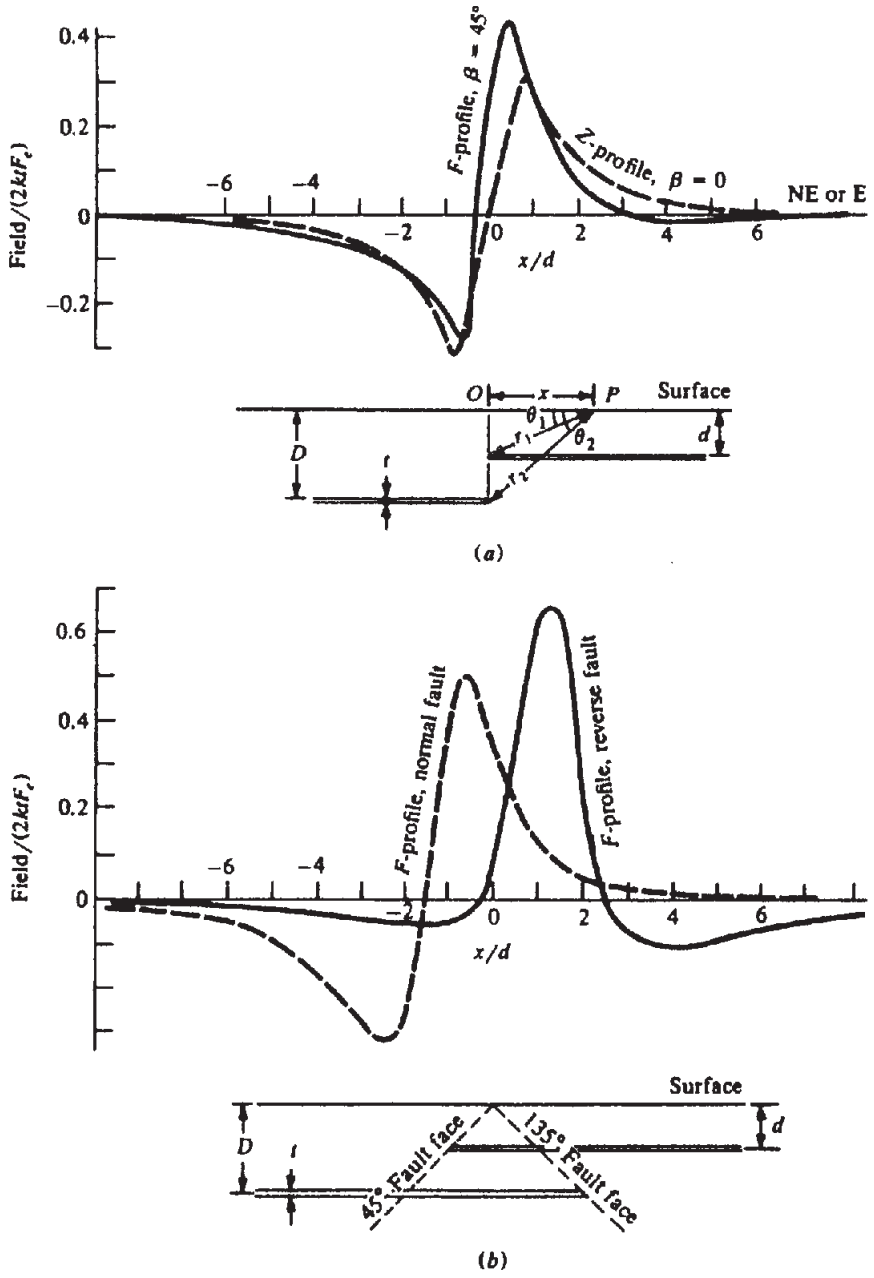

Figure 3.23. Thin-sheet fault approximation; D = 2d, I = 60°. (a) F, Z profiles for vertical faults striking N–S and SE–NW (β = 0°, 45°). (b) F profiles for normal and reverse faults striking E–W; fault dip 45, 135°.

This calculation is not simple in practice because long traverses are required to locate F_{max} and F_{min} and they are usually obscured by other anomalies.

The curve in Figure 3.25a for E–W strike is similar to profiles over dikes dipping east (Figures 3.18b and 3.20b) and it would be difficult to recognize that it represents a steeply dipping contact. In Figure 3.25b, a contact with a slant face produces a curve that gives some indication of the model. One curve (broken line) also resembles a dipping sheet; the other resembles a dipping dike.

A gradiometer profile of dF/dx defines the location of a vertical contact better than either Z or F profiles. The depth is equal to the separation of maximum and minimum values.

3.6.10. Demagnetization

In the preceding examples, we assumed that the induced magnetization is the product of k, the volume susceptibility of the body, and the external field $\mathbf{F}_e$. In fact this is true only for rod-like shapes magnetized along the axis and having a cross section small in comparison to their length, such as the dipole of Equations (3.37). In general, the resultant field inside the body is different from $\mathbf{F}_e$. This is

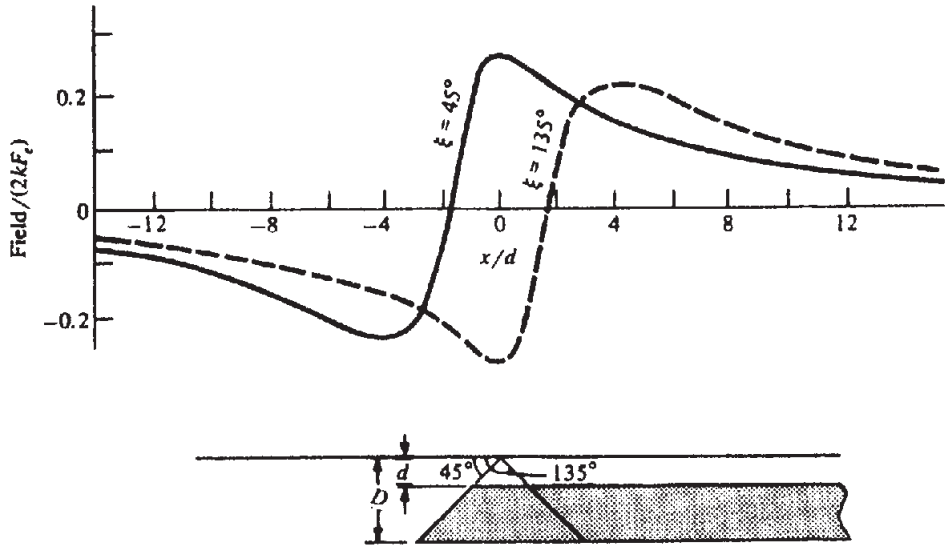

Figure 3.24. F profiles for a semiinfinite horizontal slab striking N–S, I = 45°, dip of slab terminus 45 and 135°, D = 3d.

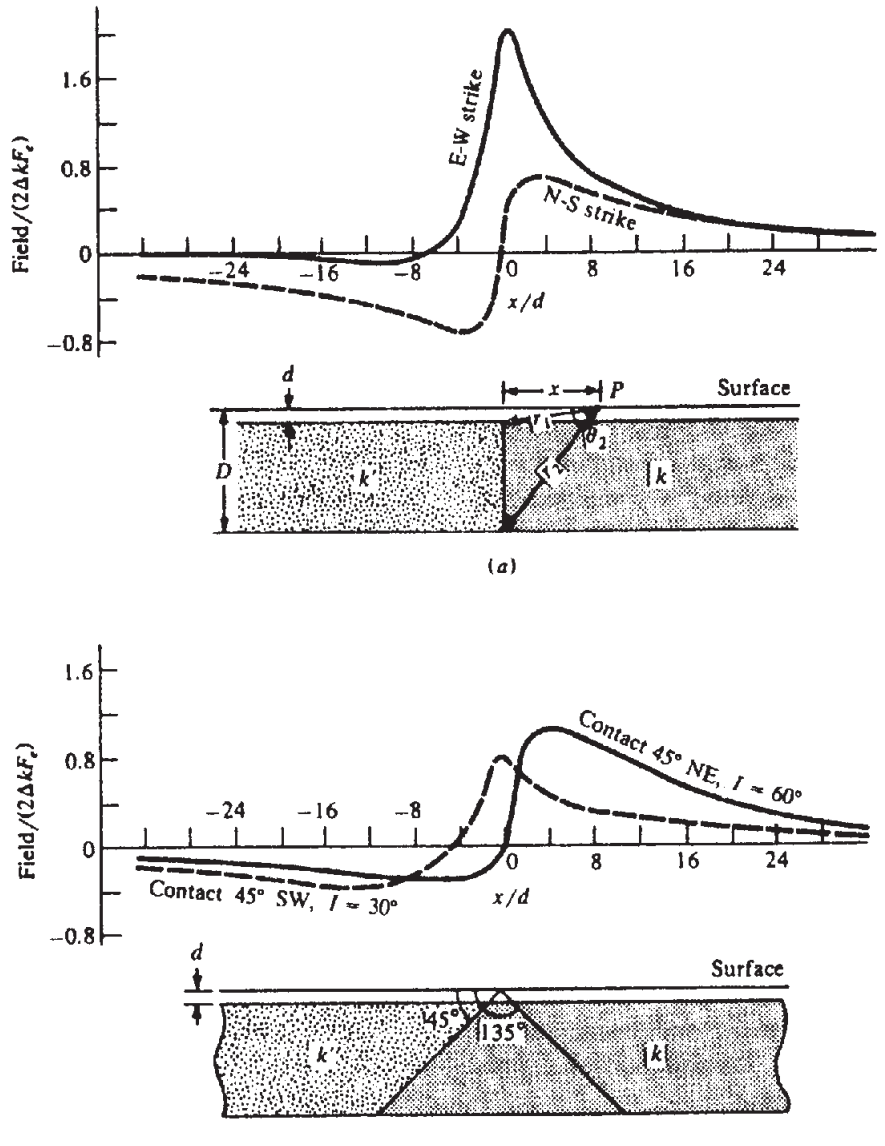

Figure 3.25. F profiles for contact between two horizontal slabs of different susceptibilities; Δk = k − k', D = 10d. (a) Vertical contact (ξ = 90°), I = 60°, β = 0 and 90°. (b) Sloping contact (ξ = 45°) for I = 30 and 60°, β = 45°.

usually called *demagnetization*. The effect can be accommodated by replacing the susceptibility k by an *apparent susceptibility* k_a:

$$k_a = k/(1 + Nk) \qquad 0 < N < 4\pi \quad (3.67)$$

Maximum demagnetization occurs in thin sheets magnetized normal to the face; in this case, $N = 4\pi$. For the sphere $N = 4\pi/3$. The effect is quite small unless $k \geq 0.1$ SI units. Demagnetization is significant only in massive pyrrhotite and in rocks containing > 5–10% magnetite. Sometimes an additional factor of $(1 - \cos^2 D \cos^2 \Delta I)$ is included to allow for the resultant magnetization being in a different direction from I; ΔI is the difference in inclination and D is the declination.

3.7. PROCESSING AND INTERPRETATION

3.7.1. General

Magnetic survey results are displayed as a set of profiles or a magnetic contour map. In sedimentary areas there may be some similarity between magnetic and gravity maps, but in general magnetic anomalies are more numerous, more erratic, less persistent, and of larger magnitude than gravity anomalies. Consequently, regional–residual separation is much more complex. Considerable success has been achieved with bandpass, matching, and nonlinear filter operators. Downward continuation is not suitable in areas of complex shallow magnetics, characteristic of mineral exploration regions. It might be used for estimating the thickness of sediments in petroleum surveys, but it is not used much for this purpose. Instead, depths are determined by semiempirical depth rules or techniques like Werner deconvolution. Second-derivative analysis is useful in mineral prospecting to enhance small-scale features near the surface, whereas upward continuation may be used to suppress them. Upward continuation may also be used to reduce topographic effects in ground magnetic work. Equation (3.33) is a crude form of upward continuation.

Aeromagnetic data are often treated as follows:

1. Reduction of data to a uniform grid by one-dimensional interpolation perpendicular to flight direction.
2. Preprocessing, which might involve continuation, calculation of derivatives, extraction of the vertical component, and so forth.
3. Summation of several profiles to attenuate background noise.
4. Filtering and setting a threshold to locate anomalous areas.
5. Analyzing the profiles for the locations and orientations of anomalies.
6. Interpolating profiles normal to strike and centered on anomalies, for more detailed analysis.
7. Comparing profiles with curves developed from models.

Comparing field measurements with the results expected for simple models, such as discussed in Section 3.6, is done to determine the location, depth, size, shape, attitude, and, possibly, the susceptibility of the magnetic bodies responsible for the anomalies. Although simplified both geometrically and with regard to magnetization, matching curves (*parametric analysis*) with model curves provides reasonably rapid analysis and may be sufficient, especially where data are poor and/or incomplete.

Considerable effort has been expended to develope workable inversion procedures for magnetics, and, in spite of the nonunique nature of the problem, several effective algorithms have been developed, to which numerous references in the literature attest (Bhattacharyya, 1964; Hartman, Teskey, and Friedberg, 1971; Al-Chalabi, 1971; McGrath and Hood, 1973; Barnett, 1976; Teskey, 1980). Werner deconvolution (§3.7.10) is one such algorithm. The conventional starting point for magnetic data inversion might be a least-squares fit, ridge regression (Leite and Leao, 1985), and so on, as in Section 2.7.9, but magnetic inversion is more complex than gravity inversion because there are more variables.

3.7.2. Crude Interpretation and Structural Aspects

Because of the erratic and complex character of magnetic maps, interpretation is often only qualitative. Indeed, interpretation is something of a fine art. An interpreter experienced in magnetics can usually see structure merely by looking at a magnetic map, much as one can visualize surface features from the contours of a topographic map. Frequently magnetic features are rather directly related to surface outcrops and a magnetic map may be a fair substitute for a surface geology map where surface features are obscured by alluvium. Often there is a connection between magnetism and topography, as well as with buried geologic structures, particularly in mineral exploration areas. A visual study of the magnetic maps can be fruitful for preliminary interpretation. In this regard, experience is essential. Remanent magnetization, however, can produce significant effects and lead to incorrect interpretation if overlooked.

In sedimentary regions, particularly where the basement depth exceeds 1,500 m, the magnetic con-

tours are normally smooth and variations are small, reflecting the basement rocks rather than near-surface features. The larger anomalies usually are caused by susceptibility variations rather than basement relief. Consequently, anomaly magnitude is not of much value in finding basement depth, and depth calculations are usually based upon anomaly shape measurements, especially sharpness.

Regions where igneous and metamorphic rocks predominate, like the Precambrian Canadian Shield and the Appalachians, usually exhibit complex magnetic variations. Deep features are frequently camouflaged by higher frequency magnetic effects originating nearer the surface. Techniques for separating deep and shallow anomalies are similar to those discussed for gravity features in Section 2.6.

Magnetic anomalies often lie in trends. From a study of aeromagnetic maps of primarily sedimentary areas in western and central North America and Venezuela, Affleck (1963) found that the dominant direction within single magnetic–tectonic provinces is usually NE–SW or NW–SE and the trend normally terminates at the province boundaries. Moderate to weak features trending E–W or N–S often are superimposed on these. These weaker trends frequently extend across province boundaries and are probably of more recent origin. A cursory study of the Canadian Appalachian region (the Maritime provinces and eastern Quebec south of the St. Lawrence) and northern Saskatchewan and Alberta appears to confirm the trends. Large-scale northeast trends are obvious on the east and west flanks of the Canadian Shield.

3.7.3. Data Processing Operations: The Fourier Transform

As with gravity and seismic data processing, mathematical operations, such as convolution and correlation, can accomplish filtering, residualizing, continuation, and so on. Operations can be performed in the spatial, or wavenumber, domain (often called the frequency domain because wavenumber is spatial frequency). Fourier transforms (§A.9) are particularly useful in magnetics for (i) resolution of specific anomalies by downward or upward continuation, (ii) changing the effective field inclination (reduction to the pole) or conversion of total-field data to vertical-component data, (iii) calculation of derivatives, (iv) general filtering – separating anomalies caused by sources of different size and depth, and (v) modeling (Bhattacharyya and Navolio 1976). For literature on transformations of potential field data, see Dean (1958), Bhattacharyya (1965, 1966), Gunn (1975), and Spector and Grant (1985).

We usually write relations using two-dimensional Fourier transforms $f(x, y) \leftrightarrow F(u, v)$ (Eq. (A.57)) in the form

$$f(x, y) = (1/2\pi)^2 \int\int F(u, v)\, e^{j2\pi(ux+vy)}\, du\, dv \tag{3.68a}$$

$$F(u, v) = \int\int f(x, y)\, e^{-j2\pi(ux+vy)}\, dx\, dy \tag{3.68b}$$

(x, y) are spatial coordinates and (u, v) are wavenumber coordinates.

The important characteristic of transformations is that information is not lost in the process, and in many cases operations are easier to perform in the transform domain. For example, the output–input expression $g(x, y) \rightarrow f(x, y) * w(x, y)$ for convolution in the spatial domain is (§A.10)

$$g(x, y) = \int\int f(x - \alpha, y - \beta)\, w(\alpha, \beta)\, d\alpha\, d\beta \tag{3.69a}$$

where $w(\alpha, \beta)$ is the convolution operator (also called a *weighting function* or *filter*). In the wavenumber domain, this becomes simple multiplication:

$$G(u, v) = F(u, v)\, W(u, v) \tag{3.69b}$$

The relations between sources and their potential fields may be considered convolution operations, and transforms can be used to determine source characteristics from field operations, as discussed in the following sections.

3.7.4. Derivatives

Derivatives tend to sharpen the edges of anomalies and enhance shallow features. First and second vertical derivative maps are the most common ones made. Derivative maps may be made by the same techniques used for gravity data (§2.6.5). The first vertical derivative is also measured in gradiometer surveys.

3.7.5. Continuation

Field continuation was discussed in Section 2.6.7 as it applies to gravity. Adapting Equation (2.48) to magnetics, we have, for upward continuation (where z is positive downward),

$$F(x', y', -h) = \frac{h}{2\pi} \int\int \frac{F(x, y, 0)\, dx\, dy}{\left\{(x - x')^2 + (y - y')^2 + h^2\right\}^{1/2}} \tag{3.70}$$

Table 3.2. *Coefficients for upward continuation.*

i	r_i	$K(r_i,1)$	$K(r_i,2)$	$K(r_i,3)$	$K(r_i,4)$	$K(r_i,5)$
0	0	0.11193	0.04034	0.01961	0.01141	0.00742
1	1	0.32193	0.12988	0.06592	0.03908	0.02566
2	√2	0.06062	0.07588	0.05260	0.03566	0.02509
3	√5	0.15206	0.14559	0.10563	0.07450	0.05377
4	√8	0.05335	0.07651	0.07146	0.05841	0.04611
5	√13	0.06586	0.09902	0.10226	0.09173	0.07784
6	5	0.06650	0.11100	0.12921	0.12915	0.11986
7	√50	0.05635	0.10351	0.13635	0.15474	0.16159
8	√136	0.03855	0.07379	0.10322	0.12565	0.14106
9	√274	0.02273	0.04464	0.06500	0.08323	0.09897
10	25	0.03015	0.05998	0.08917	0.11744	0.14458

The left side is the total field at the point $P(x', y', -h)$ above the surface on which $F(x, y, 0)$ is known. The calculation procedure is to replace the integral with a weighted sum of values taken on a regular grid.

The empirical formula of Henderson (1960) gives the field at the elevation h above the surface in terms of values $F(r_i)$, the average value $\overline{F(r_i)}$ over a circle of radius r_i centered at the point $(x, y, 0)$:

$$F(x, y, -h) = \sum \overline{F(r_i)} K(r_i, -h) \quad (3.71)$$

where $K(r_i, -h)$ are weighting coefficients (listed in Table 3.2 for $h = 1$ to 5). These coefficients give the upward continued field within 2%.

Another solution for continuation (in either direction) is by means of a Maclaurin expansion [Eq. (A.40)]:

$$\begin{aligned} F(x, y, h) = {} & F(x, y, 0) + h\, \partial F(x, y, 0)/\partial z \\ & + (h^2/2!)\, \partial^2 F(x, y, 0)/\partial z^2 \\ & + (h^3/3!)\, \partial^3 F(x, y, 0)/\partial z^3 + \cdots \end{aligned} \quad (3.72)$$

[compare with Eq. (3.33)]. For a first approximation, the first two terms involving F and $\partial F/\partial z$ are often sufficient, and the simultaneous measurement of total field and vertical gradient provides these values. The $\partial^2 F/dz^2$ term can be found from maps of F, as indicated in Section 2.6.5, and, if necessary, the $\partial^3 F/\partial z^3$ term can be found in a similar manner from maps of $\partial F/\partial z$.

The Fourier transform provides another technique for field continuation. The integrand in Equation (3.70) is the product of $F(x, y, 0)$ and $(h/2\pi)\{(x - x')^2 + (y - y')^2 + h^2\}^{-3/2}$. Using the symmetry theorem [Eq. (A.60)] and the convolution theorem [Eq. (A.67a)], we get

$$\begin{aligned} X(t)\, Y(t) &\leftrightarrow 2\pi x(-\omega) * y(-\omega) \\ &= 2\pi x(\omega) * y(\omega) \end{aligned}$$

Thus, applying this result and Equation (A.62), we obtain for the transform of Equation (3.70),

$$\mathcal{F}_n(u, v) = (-2\pi/uv)\, \mathcal{F}_0(u, v) * \mathcal{W}(u, v) \quad (3.73)$$

where $\mathcal{F}_h(u, v) \leftrightarrow F(x', y', -h)$, $\mathcal{F}_0(u, v) \leftrightarrow F(x, y, 0)$, and $\mathcal{W}(u, v) \leftrightarrow w(x, y) = (h/2\pi)(x^2 + y^2 + h^2)^{-3/2}$.

The continuation filter is

$$\begin{aligned} \mathcal{W}(u, v) &= (h/2\pi) \int\int (x^2 + y^2 + h^2)^{-3/2} \\ &\quad \times e^{-j2\pi(ux + vy)}\, dx\, dy \\ &= (h/2\pi)\, e^{-2\pi h(u^2 + v^2)^{1/2}} \end{aligned} \quad (3.74)$$

For upward continuation, we know $F_0(x, y, 0)$ and the unknown is $F_h(x, y, -h)$, whose transform is

$$\begin{aligned} \mathcal{F}_h(u, v) &= \mathcal{F}_0(u, v)(h/2\pi) \\ &\quad \times \exp\left\{-2\pi h(u^2 + v^2)^{1/2}\right\} \end{aligned} \quad (3.75)$$

Thus the calculation of $\mathcal{F}_h(u, v)$ is straightforward.

Hanson and Miyazki (1984) use a continuation method that is effective where surface relief is large and rocks are highly magnetic. As in gravity, upward continuation smooths the data, whereas downward continuation emphasizes high frequencies.

3.7.6. Spectral Analysis

The Fourier transform expresses a magnetic field as an integral of sine and/or cosine waves, each defining a wave of amplitude $A(\kappa)$ and phase $\phi(\kappa)$, where $\kappa/2\pi = 1/\lambda$ is the wavenumber. Plotting $A(\kappa)$ gives the amplitude spectrum and $A^2(\kappa)$ gives the power spectrum.

The expression for the field of an anomalous body often can be written as the product of three functions in the wavenumber domain (their convolution in the spatial domain):

(i) f_a, amplitude factor, which is equal to $(4\pi M)^2$, where M is the magnetic moment/unit volume.

(ii) f_h, the depth factor, $\exp\{-2h(u^2 + v^2)^{1/2}\}$, where h is the pole depth.

(iii) f_β, the field-orientation factor, $\{l \cos\beta + m \sin\beta)^2 + n^2 = (lu + mv)^2/(u^2 + v^2) + n^2$, where β is the angle between the body's orientation and magnetic north and l, m, and n are the direction cosines of the field $\mathbf{F}_e$.

For bodies that are large compared to their depth, we require two additional factors:

(iv) The size factor: for a rectangular prism, $(\sin ua \sin vb)/(ua\ vb)^2$, where $2a$ and $2b$ are the prism dimensions.

(v) The polarization-orientation factor involving the direction cosines of the polarization vector.

We thus write the field of a point pole or dipole in terms of factors (i) to (iii) as

$$F(x, y, 0) = f_a(x, y) * f_h(x, y, h) * f_\beta(x, y) \tag{3.76a}$$

or, in the wavenumber domain,

$$\mathcal{F}(u, v, 0) = \mathcal{F}_a(u, v)\,\mathcal{F}_h(u, v, h)\,\mathcal{F}_\beta(u, v) \tag{3.76b}$$

The effect of any of these factors may be removed by deconvolving in the space domain or by dividing in the wavenumber domain.

Numerous other filter operations can be used to separate deep from shallow, large from small, and three-dimensional from two-dimensional effects. Gunn (1975) discusses a solution for the magnetized rectangular prism. Hahn, Kind, and Mishra (1976) estimate depth from Fourier spectra.

3.7.7. Reduction to the Pole

This operation changes the actual inclination to the vertical. It can be performed (Baranov, 1957; Spector and Grant, 1985) by convolving the magnetic field with a filter whose wavenumber response is the product of a polarization-orientation factor and the field-orientation factor in items (v) and (iii) of Section 3.7.6. This transformation simplifies total-field maps and is a relatively easy operation at high magnetic latitudes where $Z \approx F$, but becomes more difficult near the magnetic equator (Silva, 1986).

3.7.8. Use of Master Curves for Dikes of Great Depth Extent

It is often difficult to establish a background or datum level for magnetic measurements and to locate a dike with respect to the profile. Hence, matching field results with profiles obtained from simple shapes can be difficult. An analysis (Koulomzine, Lamontagne, and Nadeau, 1970) for prisms and dikes of infinite depth extent solves this problem with master (or characteristic) curves that give depth, dip, and width of a prism or dike.

We rewrite Equation (3.44a) making the width $2b$ instead of b (Fig. 3.18a) and shifting the origin to a point above the midpoint of the top of the dike. If we assume infinite depth extent so that $r_2 = r_4 = \infty$, $\phi_2 = \phi_4$, we have

$$\begin{aligned} Z = 2kF_e \sin\xi \{ &(\cos I \sin\xi \sin\beta \\ &+ \sin I \cos\xi) \ln(r_3/r_1) \\ &+ (\cos I \cos\xi \sin\beta \\ &- \sin I \sin\xi)(\phi_1 - \phi_3) \} \end{aligned}$$

where $r_1^2 = d^2 + (x + b)^2$, $r_3^2 = d^2 + (x - b)^2$, $\phi_1 = \cot^{-1}(x + b)/d$, and $\phi_3 = \cot^{-1}(x - b)/d$. Dividing by d to obtain the dimensionless parameters $X = x/d$ and $B = b/d$, we obtain

$$\begin{aligned} Z = M\{ &\cot^{-1}(X + B) - \cot^{-1}(X - B) \} \\ &+ (N/2) \ln\left[\{ (X - B)^2 + 1 \} \right. \\ &\left. / \{ (X + B)^2 + 1 \} \right] \end{aligned} \tag{3.77}$$

where

$$M = 2kF_e \sin\xi \{ (\cos I \sin\beta \cos\xi - \sin I \sin\xi) \}$$

and

$$N/2 = 2kF_e \sin\xi \{ (\cos I \sin\beta \sin\xi + \sin I \cos\xi) \}$$

The first term is the symmetric component S and the second term is the antisymmetric component A. Over the center of the dike, S has a maximum and $A = 0$.

If we chose two conjugate points X_1 and X_2 on the dike profile such that the sum of the Z values is equal to Z_0, the value of Z at $X = 0$, that is,

$$Z_1 + Z_2 = Z_0 \tag{3.78}$$

Then, because

$$(S_1 + A_1) + (S_2 + A_2) = (S_0 + A_0) = S_0$$

we have

$$S_1 + S_2 = S_0 = Z_0 \qquad A_1 + A_2 = 0 \tag{3.79}$$

For the antisymmetric component,

$$\begin{aligned} &\ln\left[\{ (X_1 - B)^2 + 1 \} / \{ (X_1 + B)^2 + 1 \} \right] \\ &\quad + \ln\left[\{ (X_2 - B)^2 + 1 \} \right. \\ &\qquad \left. / \{ (X_2 + B)^2 + 1 \} \right] = 0 \\ &\{ (X_1 - B)^2 + 1 \} \{ (X_2 - B)^2 + 1 \} \\ &\quad = \{ (X_1 + B)^2 + 1 \} \{ (X_2 + B)^2 + 1 \} \end{aligned}$$

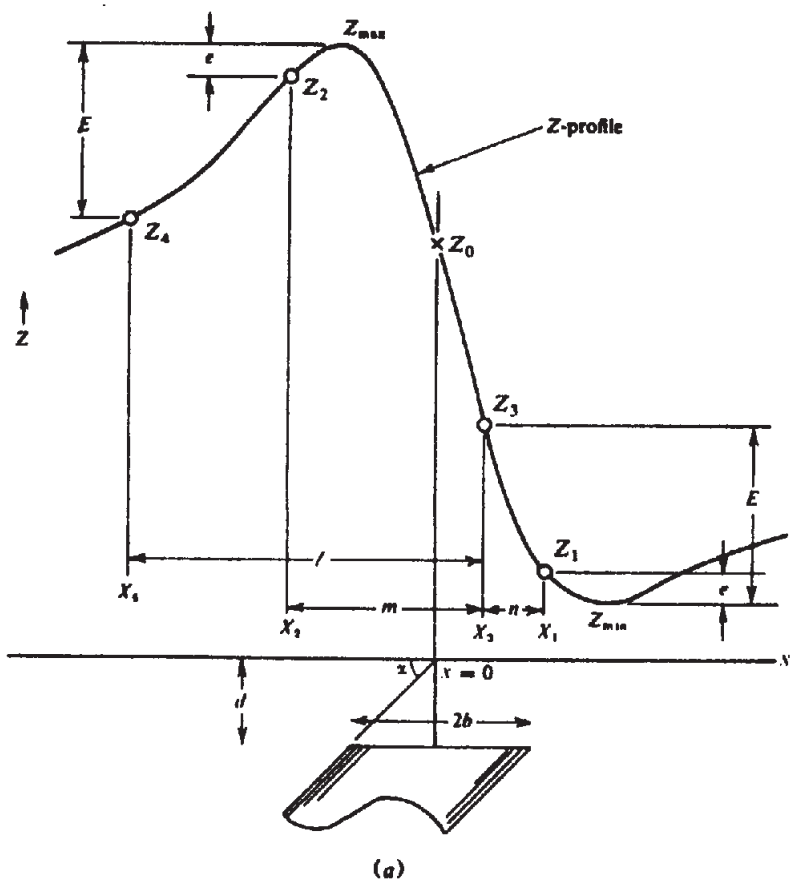

Figure 3.26. Two-dimensional dike of infinite depth extent. (a) Location of conjugate points and X = 0.

Solving for X_1X_2, this gives

$$X_1X_2 = -(1 + B^2) \tag{3.80}$$

Initially we do not know either the location of the dike center, $X = x = 0$, or the datum level $Z = 0$. Two pairs of conjugate points, X_1, X_2 and X_3, X_4, are chosen such that Equation (3.78) is satisfied, and, in addition, $Z_{max} - Z_2 = Z_1 - Z_{min} = e$ and $Z_{max} - Z_4 = Z_3 - Z_{min} = E$ (Fig. 3.26a). Writing $l = X_3 - X_4$, $m = X_3 - X_2$, $n = X_1 - X_3$, and using the relation $X_1X_2 = X_3X_4$ [Eq. (3.74)], we find that

$$\left.\begin{aligned} X_1 &= n(n + l)/(l - m + n) \\ X_2 &= -m(l - m)/(l - m + n) \\ X_3 &= mn/(l - m + n) \\ X_4 &= (m - l)(n + l)/(l - m + n) \end{aligned}\right\} \tag{3.81}$$

We can now locate the point $X = 0$ and get Z_0. For the best accuracy, X_3 and X_4 should be located close to the midpoint of the anomaly, and X_1 and X_2 near the maximum and minimum. $Z(0)$ is the point on the profile located a horizontal distance X_3 from Z_3, X_2 from Z_2, and so forth. Thus the datum line $Z = 0$ can be drawn at a distance above Z_{min} equal to the vertical distance between Z_{max} and Z_0. This follows from Equation (3.78) if we put $Z_1 = Z_{max}$ and $Z_2 = Z_{min}$, that is, $-Z_{min} = Z_{max} - Z_0$.

The analysis may now be carried further to establish the dike parameters. First, from the definitions of symmetric and antisymmetric functions,

$$\left.\begin{aligned} S(X) &= (1/2)\{Z(X) + Z(-X)\} \\ \text{and} \quad A(X) &= (1/2)\{Z(X) - Z(-X)\} \end{aligned}\right\} \tag{3.82}$$

we can plot $S(X)$ and $A(X)$ by taking points that are equidistant either side of $X = 0$. On these profiles we mark points $S_{3/4}$, $S_{1/2}$, and $A_{1/2}$ with corresponding abscissae $X_{3/4}$, $X_{1/2}$, and $X_{e/2}$; also X_e (Fig. 3.26b). By a development similar to that used for Equation (3.81), it can be shown that

$$\left.\begin{aligned} d &= x_{1/2}(\phi^2 - 1)/2 = 2x_{1/2}D \\ 2b &= x_{1/2}\left\{4 - (\phi^2 - 1)^2\right\}^{1/2} = 2x_{1/2}W \\ d &= x_e(1 - \mu)^2/2\mu = 2x_e\mathscr{D} \\ 2b &= x_e\left\{4\mu^2 - (1 - \mu)^4\right\}^{1/2}/\mu = 2x_e\mathscr{W} \end{aligned}\right\} \tag{3.83}$$

where $\phi = x_{1/2}/x_{3/4}$, $\mu = x_e/x_{e/2}$, $D = (\phi^2 - 1)/4$, $\mathscr{D} = (1 - \mu)^2/4\mu$, $W = \{4 - (\phi^2 - 1)^2\}^{1/2}/2$, $\mathscr{W} = (1/2\mu)\{4\mu^2 - (1 - \mu)^4\}^{1/2}$, $x_{1/2} = X_{1/2}d$, and so forth. Finally, we can find the dip angle ξ

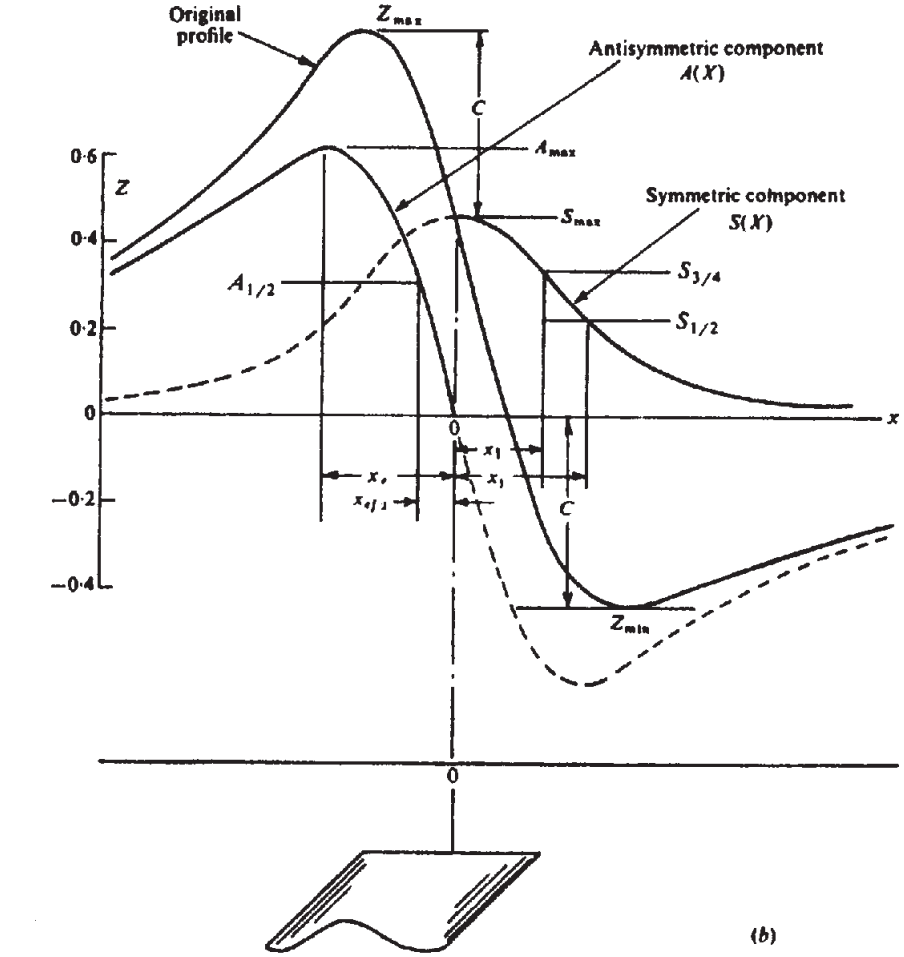

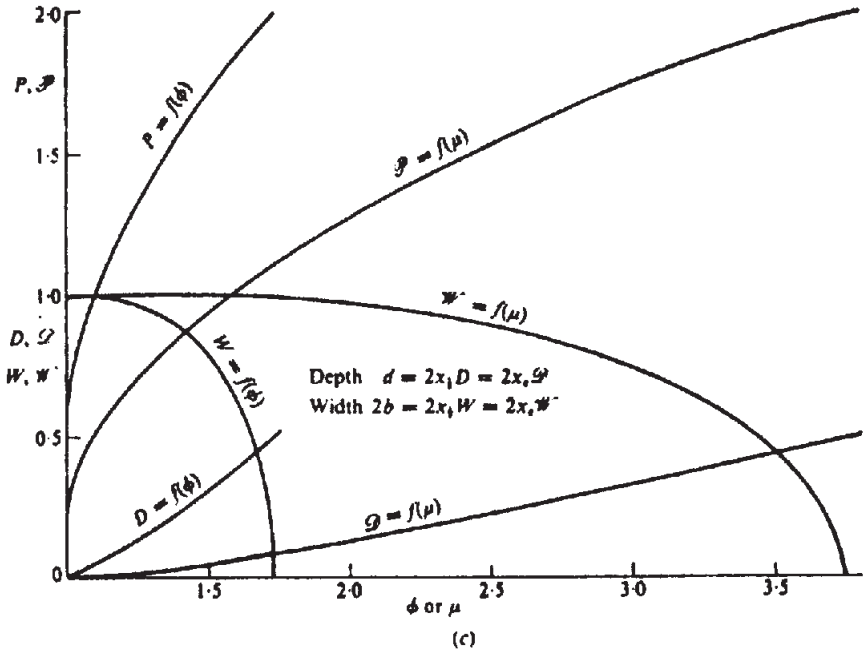

Figure 3.26. (Continued) (b) Symmetric and antisymmetric components. (c) Master curves.